Dynamic Modular Model of a Flywheel Energy Storage System

A Thesis
Presented in Partial Fulfillment of the Requirements for the
Degree of Master of Science
with a
Major in Electrical Engineering
in the
College of Graduate Studies
University of Idaho
by
David D. Arnett

Major Professor: Herbert L. Hess, Ph.D.
Committee Members: Michael Santora, Ph.D.; Christine Berven, Ph.D.;
Dakota Roberson, Ph.D.
Department Administrator: Mohsen Guizani, Ph.D.

May 2018

Authorization to Submit Thesis

This thesis of David Arnett, submitted for the degree of Master of Science with a Major in Electrical Engineering and titled "Dynamic Modular Model of a Flywheel Energy Storage System," has been reviewed in final form. Permission, as indicated by the signatures and dates below, is now granted to submit final copies to the College of Graduate Studies for approval.

Major Professor:	_____ Herbert L. Hess, Ph.D.	Date: _____
Committee Members:	_____ Michael J. Santora, Ph.D.	Date: _____
	_____ Christine A. Berven, Ph.D.	Date: _____
	_____ Dakota Roberson, Ph.D.	Date: _____
Department Administrator:	_____ Mohsen Guizani, Ph.D.	Date: _____

Abstract

High speed flywheel energy storage systems (HSFESS) can greatly benefit space and terrestrial applications. The development of HSFESS requires new materials that can withstand the forces acting on them at the speeds required for such applications. The design of a high performance machine also requires the characterization of saturation effects and adverse effects of iron on the air gap. In this thesis, a method is presented to account for the effects of non-ideal materials on machine design through the use of a composite loss factor. Also, a method is described that accounts for saturation and iron's effect on air gap permeance by reflecting these effects into the air gap of the machine. Modular modeling is proposed as a means to develop a tool for machine design that can evaluate various machine configurations without redevelopment of the model. This is accomplished by defining the machine as a collection of parameters that are used to define the physical interactions between the components of the system. Finally, finite element analysis is performed to verify the model developed.

Acknowledgements

I would like to sincerely thank Dr. Herbert Hess for his guidance and encouragement over the course of my graduate work. Dr. Hess provided me the opportunity to work on this exciting project, and for that, I am very grateful.

I would also like to extend my sincere gratitude to:

Dr. Michael Santora for his valuable knowledge and guidance on microcontrollers, programming, and control systems, and for getting me interested in this project;

Dr. Christine Berven for her willingness to ask any and all questions in the pursuit of a better understanding of the system as a whole for the entire group;

Dr. Dakota Roberson for his time and aid in reviewing this work;

Justin Pettingill, Dillon Morehouse, and Brian Peterson for their time and help developing my understanding of the system;

Matt Phillips and Shea Morison for their assistance developing a torque model.

The senior design and graduate teams for their work on the project.

Dedication

To my wife, family, and friends for keeping me going

Table of Contents

Authorization to Submit Thesis . . . ii
Abstract . . . iii
Acknowledgements . . . iv
Dedication . . . v
Table of Contents . . . vi
List of Figures . . . viii
List of Tables . . . ix
List of Abbreviations . . . x

Chapter 1: Introduction . . . 1
1.1 Thesis Objectives . . . 2
1.2 Scope . . . 3
1.3 Literature Review . . . 4

Chapter 2: Composite Materials . . . 6
2.1 Effects of Composite Materials on the Stabilization Bearing . . . 6
2.2 Effects of Composite Materials on the Drive Bearing . . . 13

Chapter 3: Iron . . . 16
3.1 The Effective Air Gap . . . 16
3.2 Saturation . . . 25

Chapter 4: Dynamic Modeling . . . 29
4.1 Torque Production . . . 29
4.2 Material Effects . . . 32
4.3 Saturation . . . 32
4.4 Mechanical Dynamics . . . 33
4.5 Model Development . . . 33

Chapter 5: Results and Verification . . . 35
5.1 Effects of Composite Materials . . . 35
5.2 Torque Production Simulation . . . 48

Chapter 6: Summary and Recommendations . . . 52
6.1 Summary . . . 52
6.2 Future Work . . . 53

References **56**

Appendix: Matlab Code for Dynamic Modular Model **58**

List of Figures

2.1 UIFESS stabilization bearing configuration, from [3] 7
2.2 A simple magnetic circuit, from [15] 7
2.3 A cylindrical magnetic circuit, from [15] 10
2.4 A gyrator-capacitor model of a simple magnetic circuit 11
2.5 UIFESS drive bearing winding schematic, from [2] 13
2.6 A Salient-Pole Machine with Rotor Eccentricities, from [18] 14

3.1 Approximate flux path due to stator slots and teeth, from [10] 17
3.2 (a) Air gap permeance due to slot openings, (b) Air gap permeance due to pole gaps, and (c) Geometry of a salient pole, from [11] 19
3.3 Flux line distribution due to stator slots and teeth 23
3.4 UIFESS drive bearing with direct and quadrature axis shown, from [2] . 26
3.5 Representation of saturation characteristic, from [14] 28

5.1 FEMM model of the UIFESS demonstrator 36
5.2 UIFESS single axis electromagnet demonstration device, from [3] 36
5.3 FEMM results of demonstrator with (a) iron floater and (b) composite floater 38
5.4 FEMM B across air gap for (a) iron floater and (b) composite floater . . 39
5.5 FEMM results for flux density under the pole face of the demonstrator . 40
5.6 FEMM model of the drive bearing using the current machine geometry . 42
5.7 FEMM results for the drive bearing with (a) an iron rotor and (b) a composite rotor 43
5.8 FEMM B across air gap for (a) iron rotor and (b) composite rotor 44
5.9 FEMM results for flux density under the pole face of the rotor 45
5.10 Flux density in the air gap of the drive bearing using the current machine geometry with an iron rotor 46
5.11 Flux density in the air gap of the drive bearing using the current machine geometry with a composite rotor 47
5.12 Flux density in the air gap of the drive bearing using the current machine geometry with a composite rotor and k_{com} fit using FEMM data 48
5.13 Electromagnetic torque on the drive bearing using the current machine geometry with an iron rotor 49
5.14 Electromagnetic torque on the drive bearing using the current machine geometry with a composite rotor 50

List of Tables

5.1 Model parameters based on demonstrator 37
5.2 Comparison of methods used to calculate B in Tesla 41
5.3 Comparison of method error against FEMM 41
5.4 FEMM torque predictions about (0,0) with the electrical angle increasing in a clockwise direction 51

List of Abbreviations

FEA	Finite Element Analysis
FEM	Finite Element Method
FEMM	Finite Element Method Magnetics
FESS	Flywheel Energy Storage System
HSFESS	High Speed Flywheel Energy Storage System
MMF	Magnetomotive Force
NASA	National Aeronautics and Space Administration
UIFESS	University of Idaho's Flywheel Energy Storage System

Chapter 1

Introduction

There are efforts being made by NASA to colonize the lunar surface. These efforts are being made with several goals. Two of these goals stand out in the context of this work: developing strategies for improving the success of future explorations further into space and increasing the scientific knowledge of the history of earth and the universe [1].

In order to explore the lunar surface and perform scientific experiments, the lunar colony will require a substantial amount of energy. There are many ways to generate energy, but two stand out as applicable due to the resources available on the lunar surface.

The first is some form of fuel turbine generation in which a fuel is consumed to spin a turbine connected to an electric generator. For a lunar application, the most cost effective fuel to use is nuclear due to its high energy density. Also, nuclear generation does not require oxygen for combustion which reduces the amount of oxygen that has to be shipped to the colony. One advantage of this type of generation is the ability to store energy in the form of unspent fuel. The major downside to this type of energy generation is the need for the construction of a plant. This might seem like an obvious statement, but all aspects of the plant construction need to be considered along with the added shipping cost.

To deliver all of the materials needed to construct a power plant plus the necessary equipment and personnel to perform the construction would be an enormous cost. Also, it should be pointed out that all of the equipment would need power to operate.

The second source of energy generation is photovoltaics. This seems like an ideal method of energy generation, as NASA often uses photovoltaics to power various aspects of missions. Also, solar generation systems require little maintenance after installation.

The use of a solar generation system for a colony's energy needs on the lunar surface provides an interesting technical challenge. The phase cycle of the moon is 708 hours on average, meaning that the moon has 354 hours of sunlight followed by 354 hours of darkness. Solar generation can only take place when the photovoltaic cells are in the sunlight. Then, the challenge is to provide energy during the other 354 hours.

It would also be possible to install a second solar generation system on the opposite side of the lunar surface. This is not an optimal solution due to the additional cost and the large distance the energy would need to travel.

Many energy storage systems have been developed. Such systems include: chemical energy storage systems, like batteries and fuel cells, electrical energy storage systems, like super capacitor systems, and mechanical energy storage systems, like flywheels. The various benefits of such systems have been explored for this type of system in [2], [3], and [4]. The architecture chosen for a lunar colonization application was a flywheel energy storage system due to its favorable energy density.

The flywheel energy storage system (FESS) being developed by the University of Idaho is an inside-out field regulated reluctance machine. This machine topology was chosen due to the theoretical viability of very low operational losses resulting in very long term energy storage [2]. The goal of this development is to investigate and improve the energy storage capability of flywheel energy storage systems in support of human colonization of the lunar surface.

1.1 Thesis Objectives

The work by Justin Pettingill [5] indicates the potential use of materials that are not ideal when considering electromagnetic machine design. These materials tend to have high strength, making them ideal from a mechanical design perspective, but low permeability. These materials are being considered to capitalize on the fact that the kinetic energy stored in a flywheel increases quadratically with angular velocity. This is seen in the kinteic energy function of a flywheel:

$$E_k = \frac{1}{2} J \omega^2 \tag{1.1}$$

where J is the moment of inertia of the rotating body.

Previous models of the UIFESS, developed by Bridget Wimer [2] and Brent Kisling [3], made the usual assumption that iron has a high enough permeability and can hence be ignored in the machine equations. These models are developed using amperes law and modified winding theory to predict the magnetomotive force (MMF) produced by the machine coils. The MMF is then used to predict the force that the stator can produce to move the rotor. This is a crucial first step to the development of this type of machine due to the hubless machine architecture chosen for the UIFESS. This makes these works an appropriate first step in the modeling of the machine.

In order to develop a high speed FESS (HSFESS), where the machine operates close to the design limitations, these idealized models must be made more realistic. This body of work is primarily intended to explore key electromagnetic concerns when developing a HSFESS. This exploration involves developing methods to quantitatively

determine the effects of non-ideal materials, like composite materials, being used to construct the machine rotor. Also, a method of including machine saturation and iron effects is discussed due to the demands of a high performance machine. The results of these methods are presented with finite element analysis (FEA) verification.

To aid in the development of the University of Idaho's HSFESS, a modular modeling technique is discussed, and preliminary results are provided. This modeling approach is performed with regard to torque production but can be expanded to include the bearing forces from [2] and [3].

1.2 Scope

The work described in this thesis was performed between August 2016 and May 2018. During that time, several graduate researchers collaborated on the project. This research was funded by the Phase III of the Steckler Space Grant provided by NASA. Phases I and II of the project were performed by Bridget Wimer [2], Brent Kisling [3], and Kevin Ramus [4]. The goal of these two phases was the research and development of a proof of concept low speed FESS using an integrated, hubless flywheel to design and test control algorithms including degaussing schemes. Phase III is aimed at evaluating the performance of the low speed FESS and designing, building, and testing a HSFESS. To aid in the organization of project knowledge, a list of the primary results of each thesis is included:
This thesis:

- Electromagnetic modeling of composite material
- Machine performance with non-ideal iron
- Modular modeling with torque production

Justin Pettingill [5]:

- Composite material behavior
- Mechanical properties of composites
- Rotor modeling

Brenden Kaschmitter [6]:

- Cylindrical stress modeling

- Multiple ring flywheel modeling
- Optimization to reduce deflection and improve energy storage

Bridget Wimer [2]:

- Field regulated reluctance machine design
- Magnetic bearing force derivation
- FESS translational dynamic model

Brent Kisling [3]:

- Axial control of a self-bearing machine
- Rotational control of a self-bearing machine
- Stabilization design and control using active magnetic bearings

Kevin Ramus [4]:

- Power electronics for the UIFESS
- Sensor selection, testing, and characterization
- Vacuum system selection

1.3 Literature Review

In the last two decades, electric machine design has begun to incorporate composite materials. The benefits of incorporating soft magnetic composite materials in machines are reduced eddy currents, reduced machine weight, and improved manufacturability [7][8][9].

In [7], composite materials are used to maintain the position of magnets in a permanent magnet machine. These materials are being considered due to the machine's high rotational speed of 50,000 RPM which could result in the magnets detaching from the rotor [7]. Another application of composite materials is presented in [8], where the composite materials are being used to construct the rotor of a permanent magnet machine. The primary purpose of this method is to reduce the weight of the machine by replacing the rotor laminations with a soft magnetic composite material [8]. The work

presented in [9] focused on developing a machine core for a permanent magnet machine. Soft magnetic composite materials were being used to develop stator geometries, that are not possible with traditional iron laminations, with reduced manufacturing costs.

The inclusion of iron effects in machines is well researched and documented. The works of [10], [11], and [12] present methods for including the permeance of the air gap due to iron in torque calculations. In [10], an approximation of this permeance is used to develop an effective air gap. In [11], a more accurate approximation of the air gap permeance is developed using FEA results. The approach presented in [12] is to approximate the length of the flux path to infer the effect of the iron by increasing the air gap by the approximate flux path length.

One method of incorporating the saturation in machine models is based on the notion that saturation is largely going to be manifested in a third harmonic component[13]. A method of approximating the saturation coefficient is presented from [14].

Chapter 2

Composite Materials

The future of the UIFESS is dependent upon the energy capacity of the system. The first iteration of a high speed UIFESS is intended to store energies that are orders of magnitude greater than the current system. In order to achieve this goal, the mechanical constraints have been explored in [5] and [6].

One proposed solution to achieve higher rotational velocities is explored in [5] which includes the use of composite materials. If these composite materials are used in the inside surface of the rotor, where the material will interact with the magnetic field of the machine, a method of accounting for the magnetic properties of the materials needs to be considered. This is the case if the machine is to be designed with a composite rotor composed of iron, matrix, and carbon fiber as described in [5].

The electrical limitations are evident in the permeability of the materials. The permeability of the composites is found to be much less than that of the iron due to the air gap effect created by the matrix and carbon fibers. This reduction in permeability affects both the machine's ability to produce correctional forces and torque.

Throughout this thesis the analysis of machines is presented using two machine architectures: one with a rotor in the center and one with a stator in the center. These two architectures are analyzed in an interchangeable fashion due to the underlying physics of the analysis which is Ampere's Law. This method of analysis is concerned with the flux path which is not dependent on the order in which the materials and media are encountered.

2.1 Effects of Composite Materials on the Stabilization Bearing

The effect on the forces produced by the stabilization bearing is expressed through the force equation derived from amperes law or magnetic equivalent circuits. This approach is valid, because the rotor portion of the stabilization bearing is a uniform surface (i.e. no chevrons), and the stator portion has few teeth with no shared coils. This configuration is shown in Figure 2.1. The configuration of the stabilization bearing can be reduced to four decoupled equivalent magnetic circuits. Each circuit is represented using a simpler circuit like the one shown in Figure 2.2.

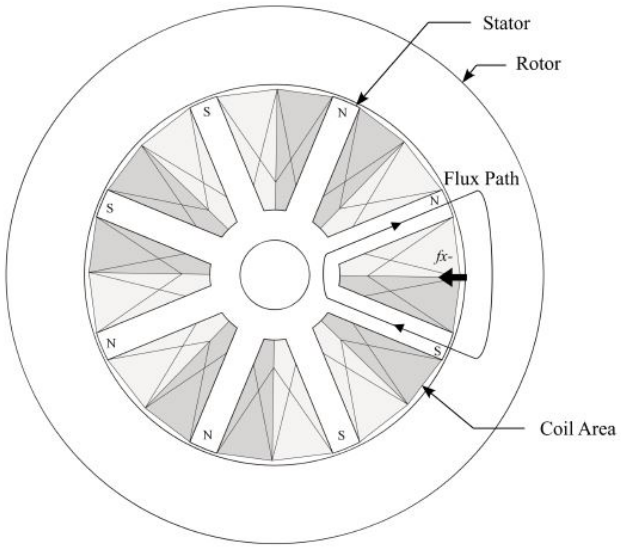

Figure 2.1: UIFESS stabilization bearing configuration, from [3]

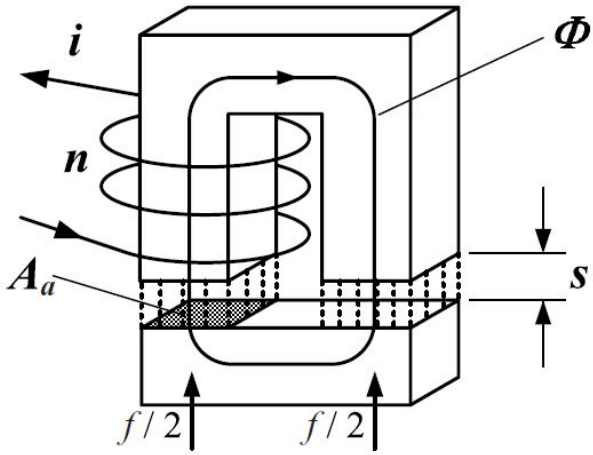

Figure 2.2: A simple magnetic circuit, from [15]

The magnetic circuit in Figure 2.2 is created with the assumption that the horseshoe and floater are composed of iron. The assumptions that the two components are iron and that the permeability of iron is always much greater than 1 leads to the derivation presented in [2] and [3]. This derivation results in the simplification of (2.1) into (2.2). In the ensuing discussion, ni or magnetomotive force (MMF) is represented as NI. Other points on notation in the following equations:

- l is the length of the flux path (Φ), shown in Figure 2.2, through some material or medium
- the subscript fe indicates the variable of concern is being measured in iron
- the subscript a indicates the variable of concern is being measured in air
- the subscript c indicates the variable of concern is being measured in composite
- μ_0 is the permeability of vacuum
- μ_x is the relative permeability of the material of concern (x)
- B is flux density
- A_x is the cross sectional area through which flux penetrates the surface of material x.

$$B = \mu_0 \frac{NI}{\left(\frac{l_{fe}}{\mu_{fe}} + 2s\right)} \tag{2.1}$$

$$B = \mu_0 \frac{NI}{2s} \tag{2.2}$$

If the horseshoe and the floater are not made of the same material, then the equations need to be modified starting with (2.3), where the floater is assumed to be made of a composite material. This composite floater is incorporated into Ampere's Law by including the composite floater length (l_c) times the magnetic field strength in the composite floater (H_c).

$$\oint_l \bar{H} \cdot d\,\bar{s} = l_{fe}H_{fe} + 2sH_a + l_cH_c = NI \tag{2.3}$$

By assuming that the flux follows a path within the magnetic loop and that the cross sections of each material are equal, the flux density is computed from the following equations [15], where

$$\Phi = A_{fe}B_{fe} = A_aB_a = A_cB_c \tag{2.4}$$

and, for the idealized horseshoe configuration,

$$A_{fe} = A_a = A_c \tag{2.5}$$

therefore

$$B_{fe} = B_a = B_c = B. \tag{2.6}$$

It is important to understand the assumptions above. The assumption is being made that no flux is escaping the material and the flux in the air gap is confined within the envelope of the cross sectional area. This assumption removes the effects of cornering, fringing, and leakage flux on the flux density. Another assumption being made is that the cross sectional areas of the materials and media are equal.

Since the flux density is identical in each of the materials, the field intensities H_{fe}, H_a, and H_c from (2.3) is replaced as shown in (2.7).

$$l_{fe}\frac{B}{\mu_0\mu_{fe}} + 2s\frac{B}{\mu_0} + l_c\frac{B}{\mu_0\mu_c} = NI \tag{2.7}$$

Solving (2.7) for B yields

$$B = \mu_0\frac{NI}{\left(\frac{l_{fe}}{\mu_{fe}} + 2s + \frac{l_c}{\mu_c}\right)}. \tag{2.8}$$

From (2.8) and (2.1), it is clear that B (with a composite in the loop) is equivalent to B (with only iron and air in the loop) multiplied by a composite loss factor (k_{com}):

$$k_{com} = \frac{\left(\frac{l_{fe}}{\mu_{fe}} + 2s\right)}{\left(\frac{l_{fe}}{\mu_{fe}} + 2s + \frac{l_c}{\mu_c}\right)} \tag{2.9}$$

This allows a system containing composite materials in the magnetic circuit to be modeled as an ideal system then corrected using the composite loss factor. This is beneficial in terms of modeling because k_{com} is predefined based on material properties, which will simplify the computation of B and, therefore, the force.

The attraction force of an electromagnet is generated at the boundary of media or materials having differing permeabilities and is calculated based on the field energy [15]. The energy stored in the volume of the air gap (V_a) is expressed as

$$W_a = \frac{1}{2}B_aH_aV_a = \frac{{B_a}^2V_a}{2\mu_0}, \tag{2.10}$$

where

$$V_a = 2sA_a. \tag{2.11}$$

The force acting on the floater is generated by the gradient of energy stored within the air gap with respect to the width of the air gap. This is expressed as a function of

the floater displacement, which is the air gap (s), and the current through the coil (i). If the displacement (∂s) is small, the magnetic flux ($B_a A_a$) remains constant. This means that if s is increased by ∂s, the volume (V_a) increases proportionally. Since energy (W_a) is proportional to V_a, the increase in position results in an increase in energy by ∂W_a [15]. Using the principle of virtual displacement, where the system is frozen in time and one degree of freedom is displaced by a small amount [16], the force is expressed as the partial derivative of the field energy with respect to the air gap [15].

$$f = -\frac{\partial W_a}{\partial s} = \frac{{B_a}^2 A_a}{\mu_0} \tag{2.12}$$

By combining (2.12) and (2.8), the force on the floater can be expressed as a function of the coil current and air gap, 2.13).

$$f = \mu_0 A_a \left[\frac{NI}{\left(\frac{l_{fe}}{\mu_{fe}} + 2s + \frac{l_c}{\mu_c} \right)} \right]^2 \tag{2.13}$$

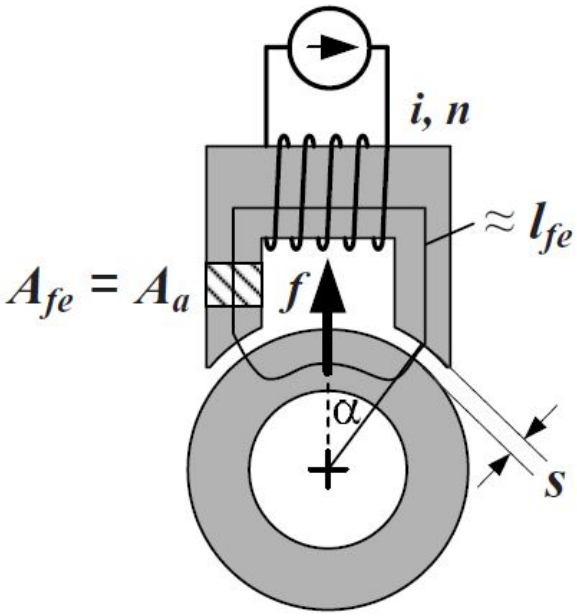

Figure 2.3: A cylindrical magnetic circuit, from [15]

This function is useful for the horseshoe configuration shown in Figure 2.2, but needs to be modified for use with a cylindrical configuration as would be used with a machine. For a curved surface, like the one shown in Figure 2.3, A_a is assumed to be the projected area of the pole face [15]. This pole face area is assumed to be much

smaller than the surface area of the cylinder that it is projected onto, which justifies using a single α value in (2.14). Also, the angle α must be considered in determining the force and is dependent on the number of poles the machine has. Equation 2.13 can be modified with these considerations to produce:

$$f = \mu_0 A_a \left[\frac{NI}{\left(\frac{l_{fe}}{\mu_{fe}} + 2s + \frac{l_c}{\mu_c} \right)} \right]^2 \cos(\alpha). \tag{2.14}$$

For this model to be used in the future of the UIFESS, it needs to be both verified and validated. Verification of the model is performed by using another magnetic circuit modeling technique to determine whether the results are appropriate under the assumptions made. The modeling technique used is the gyrator-capacitor model developed by Buntenbach in the late 1960's. This technique uses MMF ($\mathcal{F}$) as an effort variable and rate of change in flux ($\frac{d\Phi}{dt} \equiv \dot{\Phi}$) as a flow variable. Under this variable scheme, magnetic permeance ($\mathcal{P}$) is analogous to electrical capacitance, and $\mathcal{P}$ can be calculated using (2.15), where A is cross section area and ℓ is member length [17].

$$\mathcal{P} = \mu_0 \mu_r \frac{A}{\ell} \tag{2.15}$$

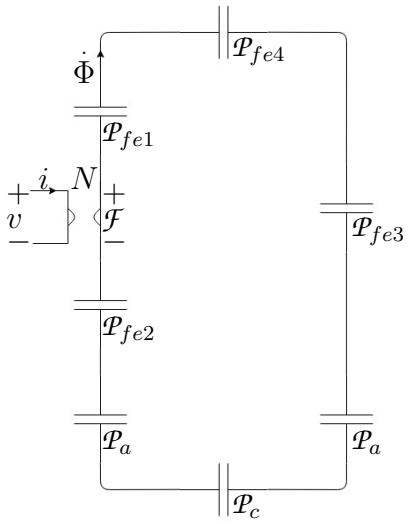

Figure 2.4: A gyrator-capacitor model of a simple magnetic circuit

The magnetic circuit shown in Figure 2.2 is represented as the gyrator-capacitor model shown in Figure 2.4, where $\mathcal{P}_{fe}$, $\mathcal{P}_a$, and $\mathcal{P}_c$ are the permeance of iron, air, and a

composite, respectively. A distinct feature of this approach is that windings are treated as two port elements linking the electrical and magnetic circuits [17]. The gyrator is described using the following equations:

$$v = N\ \dot{\Phi} \tag{2.16}$$

and

$$i = \frac{\mathcal{F}}{N}, \tag{2.17}$$

where v is the voltage across the coil, i is the current through the coil, N is the number of turns in the coil, $\dot{\Phi}$ is the first time derivative of the flux through the magnetic circuit, and $\mathcal{F}$ is the MMF produced by the coil.

Once the model is generated, it is analyzed as a capacitive circuit. In order to determine the force acting on the floater, the energy stored in the two $\mathcal{P}_a$ capacitors must be calculated; this represents the air gap energy. The energy stored in one of the air gap capacitors is calculated as:

$$W_a = \frac{1}{2}\mathcal{P}_a{\mathcal{F}_a}^2, \tag{2.18}$$

where $\mathcal{F}_a$ is the MMF across the air gap capacitor ($\mathcal{P}_a$) and is calculated as:

$$\mathcal{F}_a = \frac{1}{\mathcal{P}_a}\left[\int_{t_0}^{\tau} \dot{\Phi}\ dt\right] + \mathcal{F}_{a0}. \tag{2.19}$$

Then, the force can be calculated by taking the partial derivative of the air gap energy with respect to the change in the air gap (2.20).

$$f = -\frac{\partial W_a}{\partial s} = \frac{{B_a}^2 A_a}{\mu_0} \tag{2.20}$$

where

$$B_a = \mu_0 \frac{\mathcal{F}_a}{s}. \tag{2.21}$$

Unfortunately, the solution of this model is not as easily obtained as the previous model. The model is solved using a variety of softwares such as Mathcad®, LTspice®, and MATLAB®. The integration in this model makes it undesirable for real time simulation. If, however, there is a substantial difference in the accuracy between the two models, the increase in accuracy may justify the increase in computational cost.

2.2 Effects of Composite Materials on the Drive Bearing

The drive bearing of the machine, shown in Figure 2.5, has a more complicated configuration than the stabilization bearing. This configuration benefits from the use of modified winding theory, explained in detail in [2]. The derivation in [2] makes use of Ampere's law and assumes the components are iron and air. But, it is modified to include the effect of the path *bc*, shown in Figure 2.6, to account for a non-ideal rotor material.

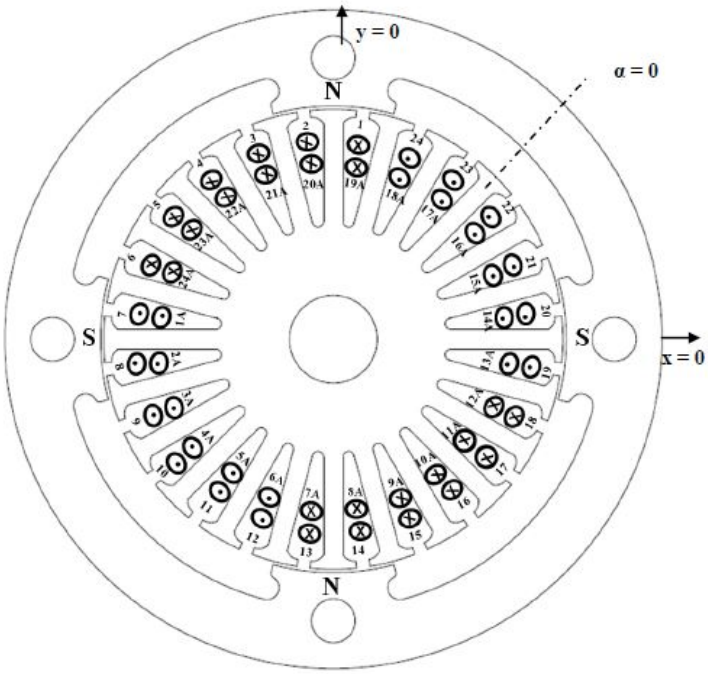

Figure 2.5: UIFESS drive bearing winding schematic, from [2]

Ampere's law is expressed as a series of $\mathcal{F}$ drops along the path *abcda*:

$$\mathcal{F}_{ab} + \mathcal{F}_{bc} + \mathcal{F}_{cd} + \mathcal{F}_{da} = n(\phi)i \tag{2.22}$$

where $n(\phi)$ is the turns function. The turns function represents the total number of turns enclosed by the path *abcda* [2].

In [2], it is shown that through the use of a modified winding function $[M(\phi)]$, the MMF is calculated at any arbitrary point in the air gap:

$$\mathcal{F}_{cd} = M(\phi)i \tag{2.23}$$

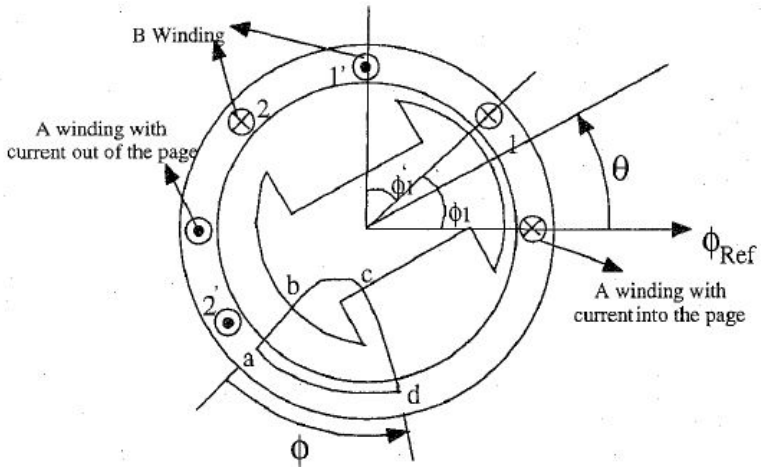

Figure 2.6: A Salient-Pole Machine with Rotor Eccentricities, from [18]

and

$$M(\phi) = n(\phi) - \frac{1}{2\pi < s^{-1}(\phi) >} \int_0^{2\pi} n(\phi) s^{-1}(\phi) d\phi, \tag{2.24}$$

where s^{-1} is the inverse air gap and $< s^{-1}(\phi) >$ is the average of the inverse air gap.

Also, discussed in [2], the force on the rotor due to the MMF is expressed as the two components $F_x(\epsilon)$ and $F_y(\epsilon)$. In these expressions, ϵ is the angle used to resolve the total force in the x and y components, r_{os} is the outer stator radius, and h_e is the effective height of the stator defined as the total height of the laminations times the stacking factor, which is the ratio of iron to insulating material:

$$F_x(\epsilon) = -\int_0^{2\pi} \left(\frac{B(\phi)^2 r_{os} h_e}{2\mu_0} \right) \cos(\phi + \epsilon) d\phi \tag{2.25}$$

and

$$F_y(\epsilon) = -\int_0^{2\pi} \left(\frac{B(\phi)^2 r_{os} h_e}{2\mu_0} \right) \sin(\phi + \epsilon) d\phi. \tag{2.26}$$

To include the effects of the non-ideal rotor material, the composite loss factor (k_{com}) needs to be defined as a function of ϕ, where ϕ is the angle represented in Figure 2.6:

$$k_{com}(\phi) = \frac{((l_{fe}/\mu_{fe}) + s(\phi_0) + s(\phi))}{\left((l_{fe}/\mu_{fe}) + s(\phi_0) + s(\phi) + \left[\left(\int_{\phi_0}^{\phi} \left[\sqrt{1 + dl_c(\varphi)^2} \right] d\varphi \right) / \mu_c \right] \right)} \tag{2.27}$$

While this expression makes sense analytically, when considering the winding function derivation, FEM results in section 5.1 show that this is not accurate. In the interpole

region the calculation of the MMF is more heavily dependent on the permeability of air than the material due to the large air gap. To improve the accuracy of the result of (2.27) a piecewise definition is useful:

$$k_{com}(\phi) = \begin{cases} k_{com}(\phi + \alpha_{rp}) & \phi < 0 \\ k_{com}(\phi - \alpha_{rp}) & \phi \geq (1.1)\alpha_{rp} \\ \frac{\left((l_{fe}/\mu_{fe})+2s(\phi_0)\right)}{\left((l_{fe}/\mu_{fe})+2s(\phi_0)+(l_c/\mu_c)\right)} & \phi < \alpha_{rp}/2 \\ 0 & \alpha_{rp}/2 \leq \phi < (\frac{2\pi}{N_p} - (1.1)\alpha_{rp}) \\ \frac{\left((l_{fe}/\mu_{fe})+2s(\phi_0)\right)}{\left((l_{fe}/\mu_{fe})+2s(\phi_0)+(l_c/\mu_c)\right)} & (\frac{2\pi}{N_p} - (1.1)\alpha_{rp}) \leq \phi < \alpha_{rp} \end{cases}, \tag{2.28}$$

where α_{rp} is the rotor pole arc, and N_p is the number of poles for the machine. Note that the air gap at ϕ is not included in this version of k_{com}, since the function is only concerned with the length of the material (l_c) extending from the pole face to the center of the rotor over to the next pole face. The flux density near the pole edges is dependent upon the material of the pole; this is accounted for by multiplying α_{rp} with 1.1. Further improvement could be achieved by multiplying k_{com} by a Fourier series tailored to the specific geometry found by using FEM to determine the number of components in the series.

For a high speed flywheel to be designed, the rotor must be capable of high rotational velocities and withstanding the increased stress caused by the increased velocity. The proposed method of constructing such a flywheel is to incorporate a strong composite material into the rotor. The use of a composite loss factor in the machine model will allow the effects of the composite materials to be quantified. Using this, the engineers responsible for machine design and control system design can account for the effects of the composite while using traditional modeling techniques.

Chapter 3

Iron

The effects of iron are often assumed to be insignificant in initial machine designs. This was also the case in the initial design of the UIFESS stabilization and drive bearings. In [2] and [3], the representation of the stabilization bearing is defined as discussed in the last chapter. In both of these derivations, the permeability of iron is assumed to be large enough for l_{fe}/μ_{fe} to be negligible. In [2], the drive bearing derivation makes the same assumption about the permeability of iron. This leads to the MMF drop across the iron of the rotor and stator to be assumed to be zero.

The previous models of the machine also neglect the effects of saturation on the machines performance. This was done because the machine was over designed to meet design goals while keeping the machine well below saturation. The machine designed in [2] is capable of speeds greater than 1800 RPM if the control system is designed to account for saturation.

In order to develop a more accurate machine model and a higher performance machine, the effects of iron in the machine need to be considered.

3.1 The Effective Air Gap

One method used to account for iron is to define an effective air gap. This effective air gap accounts for the iron path lengths described in the derivation of the composite loss factor defined in Chapter 2. These effects should be considered, since the gap length s is very small compared to the length of iron in the flux path. The effective air gap due to the stator ($s_e s$) is found by [10]:

$$s_{es} = \frac{\mu_0 \tau_s h_e}{\mathcal{P}_s}, \tag{3.1}$$

where τ_s is the stator slot pitch width and h_e is the effective height of the machine. The effective height of the machine is determined by the construction of the machine and the height of the rotor and the stator. In this model, the effective height is assumed to be equal to the height of the machine stator.

The effective air gap due to the stator can alternately be defined using a Carter factor for the stator (k_{cs}) and the nominal air gap (s) [10] is

$$s_{es} = k_{cs} s. \tag{3.2}$$

By combining (3.1) and (3.2), the Carter factor is calculate for the stator as:

$$k_{cs} = \frac{\mu_0 \tau_s h_e}{\mathcal{P}_s} s. \tag{3.3}$$

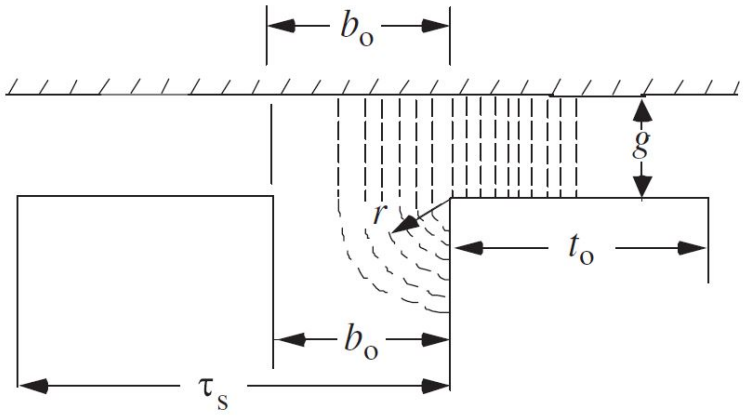

Figure 3.1: Approximate flux path due to stator slots and teeth, from [10]

In order to determine the stator Carter factor and, consequently, the effective air gap due to the stator, the permeance of the air gap due to the slot openings is needed. In [10], a method of approximating the air gap permeance is presented. This approximation assumes that the flux lines enter the slots following the path shown in Figure 3.1. Using this approximation, the Carter factor for the stator is calculated as:

$$k_{cs} = \frac{\tau_s}{\tau_s - b_o + \frac{4g}{\pi} \ln\left[1 + \frac{\pi}{4}\frac{b_o}{g}\right]}, \tag{3.4}$$

where b_0 is the slot opening and g is equivalent to s as the nominal air gap.

This approximation can then be applied using the stator geometry and the rotor geometry to develop the Carter factor for the stator (k_{cs}) and rotor (k_{cr}). The Carter factor for the machine can be defined as:

$$k_c = k_{cs} k_{cr}, \tag{3.5}$$

where k_{cr} is calculated using (3.4) but replacing the stator measurements with the equivalent rotor measurements.

Then, the effective air gap is found by combining (3.5) and (3.2) to get:

$$s_e = k_{cs} k_{cr} s. \tag{3.6}$$

Although this method does show the global effects of the iron on the air gap permeance of the machine, it does not show the local effects. The local effects of the iron on the air gap permeance are shown using various methods. The inclusion of the local effects should be considered, since these effects can have a large impact on the harmonic content in the forces and torques in the machine.

There are different analytical approaches to calculate the air gap permeance in electrical machines. In [11], a method of analytically determining the air gap permeance due to both the slot openings and salient poles is presented. This method is described by the equations below and referring to Figure 3.2.

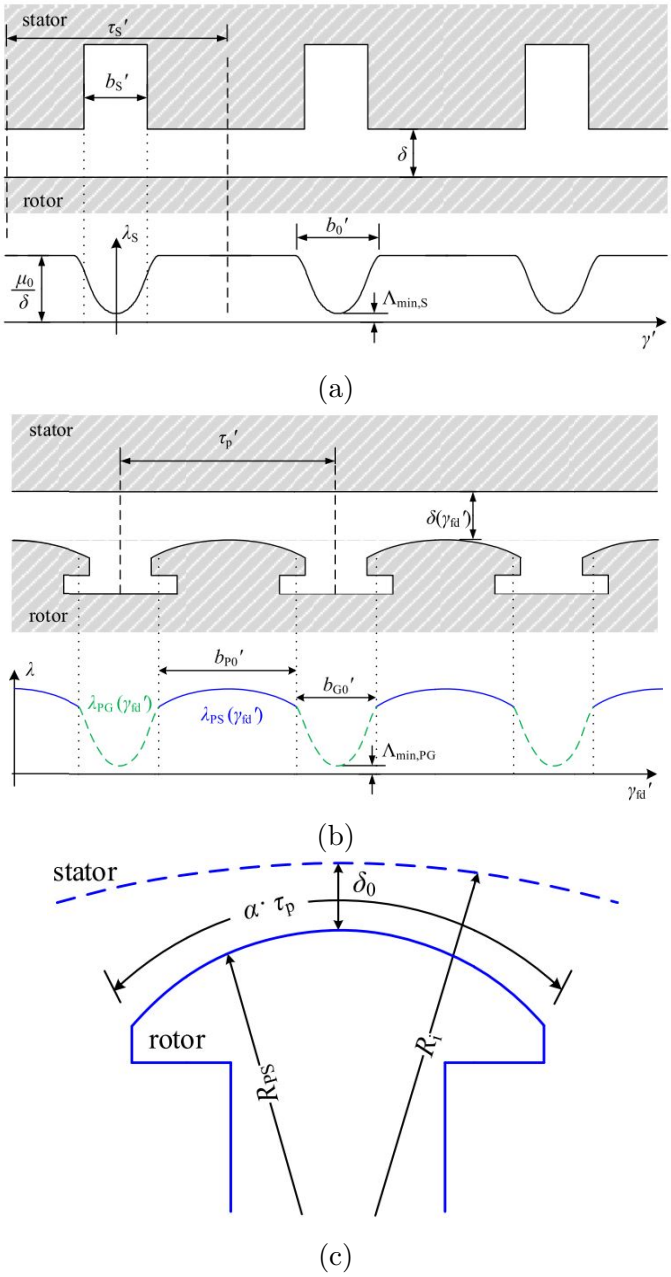

Figure 3.2: (a) Air gap permeance due to slot openings, (b) Air gap permeance due to pole gaps, and (c) Geometry of a salient pole, from [11]

For the effective permeance of the stator slots and teeth, the effective slot width (b_0'), shown in Figure 3.2 (a), needs to be considered. In this case, the air gap permeance is constant within the reduced tooth width ($\tau_s' - b_0'$) [11]. In these equations, a $'$ indicates a value measured in radians. The permeance of the half closed slots is calculated using

the Fourier decomposition[11]:

$$\mathcal{P}_{s,a}(\gamma') = \mathcal{P}_{smin,a0} + \sum_{v'} \mathcal{P}_{smin,av'} \cos\left(v'\gamma'\right), \tag{3.7}$$

where

$$\mathcal{P}_{smin,a0} = \frac{\mu_0}{\delta}\left[1 - \beta\frac{b_0'}{\tau_s'}\right] \tag{3.8}$$

and

$$\mathcal{P}_{smin,av'} = \frac{\mu_0}{\delta}\frac{\beta N_s}{v'\pi}\frac{2}{\left(\frac{v'b_0'}{2\pi}\right)^2 - 1}\sin\left(\frac{v'b_0'}{2}\right). \tag{3.9}$$

The permeance of the open slots is calculated using the Fourier decomposition as

$$\mathcal{P}_{s,b}(\gamma') = \mathcal{P}_{smin,b0} + \sum_{v'} \mathcal{P}_{smin,bv'} \cos\left(v'\gamma'\right), \tag{3.10}$$

where

$$\mathcal{P}_{smin,b0} = \frac{\mu_0}{\delta}\left[1 - \frac{11}{8}\beta\frac{b_0'}{\tau_s'}\right] \tag{3.11}$$

and

$$\mathcal{P}_{smin,bv'} = \frac{\mu_0}{\delta}\frac{\beta N}{8v'\pi}\left[\frac{15}{1-\left(\frac{2\pi}{v'b_0'}\right)^2} + \frac{6}{1-4\left(\frac{2\pi}{v'b_0'}\right)^2} + \frac{1}{1-9\left(\frac{2\pi}{v'b_0'}\right)^2} - 22\right]\sin\left(\frac{v'b_0'}{2}\right). \tag{3.12}$$

The amplitudes belonging to the air gap permeance due to the slot openings of the stator comply with the condition [11]:

$$v' = g_1 N_s \wedge f_{v'} = 0 \quad \forall\, g_1 \in \mathbb{N}_0. \tag{3.13}$$

The term N_s is the number of stator slots, and the term β (3.14) is the drop of the magnetic field density in the middle of the slots. The functions also require the effective slot width (b_0') (3.15).

$$\beta = \frac{1}{2} - \frac{1}{\sqrt{4 + \left(\frac{b_s}{\delta}\right)^2}} \tag{3.14}$$

$$b_0' = b_s'\left(1 + \left[0.8 + 10^{-4}\left(\frac{b_s}{\delta} - 6\right)^4\right]\exp\left(-\frac{1}{8.5}\left(\frac{b_s}{\delta} - 0.9\right)\right)\right) \tag{3.15}$$

Finally, the two portions of the permeance are combined with the weighting factor (a) to determine the total effective air gap permeance of the stator slots and teeth:

$$\mathcal{P}_s(\gamma') = a\mathcal{P}_{s,a}(\gamma') + (1-a)\mathcal{P}_{s,b}(\gamma'), \tag{3.16}$$

where

$$a = \begin{cases} \exp\left(-\frac{1}{6}\left(\frac{b_s}{\delta} - 1\right)\right) & \forall\ \frac{b_s}{\delta} \geq 10.6 \\ \sin^4\left(\frac{\pi}{2}\frac{19-\frac{b_s}{\delta}}{18}\right) & \forall\ \frac{b_s}{\delta} < 10.6. \end{cases} \tag{3.17}$$

For a rotor with a curved pole, the non-uniform air gap needs to be considered in the process of determining the effective permeance of the salient pole [11]. This geometry is represented in Figure 3.2 (c). The non-uniform air gap dictates the need to define a function to calculate the air gap length:

$$\delta(\gamma'_{fd}) = R_i - \sqrt{R_{PS}^2 + I_m^2 - 2R_{PS}I_m\cos\left(\pi - \gamma'_{fd} - \gamma^\star\right)}, \tag{3.18}$$

where

$$\gamma^\star = \arcsin\left[\frac{I_m \sin\left(\gamma'_{fd}\right)}{R_{PS}}\right] \tag{3.19}$$

and

$$I_m = R_i - \delta_0 - R_{PS}. \tag{3.20}$$

The effective pole shoe width is defined as b'_{P0}, which is based on finite element method (FEM) data calculated for various rotor pole geometries [11]:

$$b'_{P0} = 0.9\alpha\tau_p. \tag{3.21}$$

The minimum slot opening air gap permeance, shown in Figure 3.2 (c) as $\Lambda_{min,PG}$, is defined based on FEM results to be [11]:

$$\mathcal{P}_{min,PG} = \frac{\mu_0}{\delta_0}\left(1 - 2\beta_{PG}\right), \tag{3.22}$$

where

$$\beta_{PG} = \frac{1}{2} - \frac{1}{\sqrt{4 + \left(\frac{b_{SP}}{\delta_0}\right)^{1.685}}} \tag{3.23}$$

and

$$b_{SP} = (1-\alpha)\,\tau'_p\,(R_i - \delta_0)\,. \tag{3.24}$$

Then, the air gap permeance is calculated using two substitute functions. The actual air gap permeance is bounded by the two substitute functions. The first of these two functions ($\mathcal{P}_{sp,a}$) represents the upper bound on the actual air gap permeance due to the salient pole rotor [11]:

$$\mathcal{P}_{sp,a}(\gamma'_{fd}) = \begin{cases} \frac{\mu_0}{\delta(-\frac{b'_{P0}}{2})}\left[1-\beta x_{a2}\right] & \forall\ -\frac{\tau'_p}{2} < \gamma'_{fd} < -\frac{b'_{P0}}{2} \\ \frac{\mu_0}{\delta(\gamma'_{fd})} & \forall\ -\frac{b'_{P0}}{2} < \gamma'_{fd} < \frac{b'_{P0}}{2} \\ \frac{\mu_0}{\delta(\frac{b'_{P0}}{2})}\left[1-\beta x_{a1}\right] & \forall\ \frac{b'_{P0}}{2} < \gamma'_{fd} < \frac{\tau'_p}{2} \end{cases}, \tag{3.25}$$

where

$$x_{a1} = 1 + \cos\left(\frac{2\pi}{b'_{G0}}\left(\gamma'_{fd} - \frac{\tau'_p}{2}\right)\right) \tag{3.26}$$

and

$$x_{a2} = 1 + \cos\left(\frac{2\pi}{b'_{G0}}\left(\gamma'_{fd} + \frac{\tau'_p}{2}\right)\right). \tag{3.27}$$

Calculation of the air gap permeance, due to the rotor, requires the calculation of the modified value of the magnetic flux density drop (β_{SP}) at the boundary between the effective pole shoe and the effective pole gap (b'_{G0}) [11]:

$$\beta_{SP} = \frac{1}{2}\left(1 - \frac{\mathcal{P}_{min,PG}}{\frac{\mu_0}{\delta(\gamma'_{fd})}}\right) \tag{3.28}$$

and

$$b'_{G0} = \tau'_p - b'_{P0}. \tag{3.29}$$

The second substitute function ($\mathcal{P}_{sp,b}$) is developed as [11]:

$$\mathcal{P}_{sp,b}(\gamma'_{fd}) = \begin{cases} \frac{\mu_0}{\delta(-\frac{b'_{P0}}{2})}\left[1-2\beta x_{b2}\right] & \forall\ -\frac{\tau'_p}{2} < \gamma'_{fd} < -\frac{b'_{P0}}{2} \\ \frac{\mu_0}{\delta(\gamma'_{fd})} & \forall\ -\frac{b'_{P0}}{2} < \gamma'_{fd} < \frac{b'_{P0}}{2} \\ \frac{\mu_0}{\delta(\frac{b'_{P0}}{2})}\left[1-2\beta x_{b1}\right] & \forall\ \frac{b'_{P0}}{2} < \gamma'_{fd} < \frac{\tau'_p}{2} \end{cases}, \tag{3.30}$$

where

$$x_{b1} = 1 + \cos\left(\frac{2\pi}{b'_{G0}}\left(\gamma'_{fd} - \frac{\tau'_p}{2}\right)\right) \tag{3.31}$$

and

$$x_{b2} = 1 + \cos\left(\frac{2\pi}{b'_{G0}}\left(\gamma'_{fd} + \frac{\tau'_p}{2}\right)\right). \tag{3.32}$$

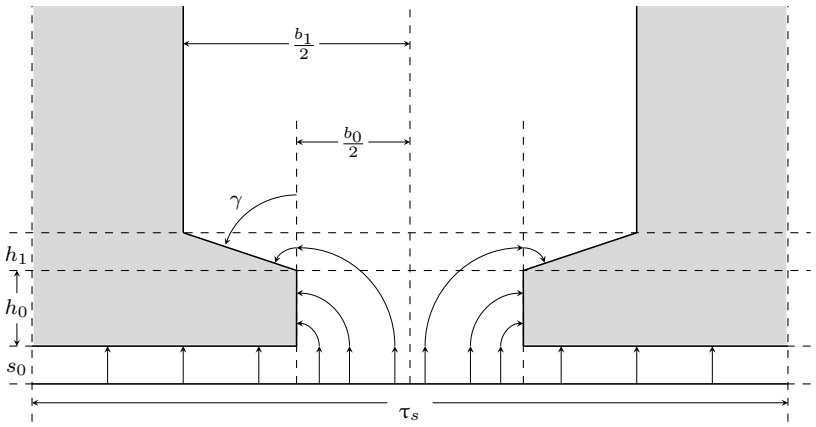

Figure 3.3: Flux line distribution due to stator slots and teeth

Finally, the air gap permeance of a salient pole rotor can be calculated by combining the two substitute functions with a modified weighting factor (a_{sp}) based on FEM results [11]:

$$\mathcal{P}_{sp}(\gamma'_{fd}) = a\mathcal{P}_{sp,a}(\gamma'_{fd}) + (1-a)\mathcal{P}_{sp,b}(\gamma'_{fd}), \tag{3.33}$$

where

$$a_{sp} = 5\alpha^2 - 3.97\alpha + 0.6135. \tag{3.34}$$

The current configuration of the UIFESS results in a simplification of the salient pole section, represented in Figure 3.2 (b) and (c), due to the uniform gap (δ_0) between the rotor and stator. This simplification results in the rotor portion of the air gap permeance being calculated like that of the stator slot portion of the air gap permeance, (3.7) - (3.17). The curved rotor pole (3.18) - (3.34) are included as a reference in the event that a curved rotor pole topology is used in the future designs of the device.

A more direct method of determining the effective air gap due to the stator slots and teeth is presented in [12]. This method estimates the flux path length based on the location along the azimuth of the stator in a manner that is similar to the approach in [10], described at the beginning of this section. The difference is that the flux path lengths due to the stator tooth and slot geometry are added to the nominal air gap, rather than condensing this affect to a global factor.

These flux path lengths are shown in Figure 3.3 where τ_s is the stator slot pitch, s_0 is the nominal air gap, h_0 is the thickness of the stator tooth face, h_1 is the thickness of the stator tooth taper, γ is the angle defined in (3.35), b_0 is the width of the slot opening, and b_1 is the width at the top of the slot. Although moving from left to right in Figure 3.3 represents an increase of the stator azimuthal angle in the clockwise direction,

it is convenient to convert the change in angle to a change in arc length by multiplying the arc by the outer stator radius (r_{os}).

$$\gamma = \frac{\pi}{2} - \arctan\left(\frac{h_0}{((b_1 - b_0)/2)}\right) \tag{3.35}$$

The effective air gap due to the stator geometry is then defined as a repeating pattern of

$$s_s(\theta_m) = \begin{cases} s_s(\theta_m + \alpha_{sp}) & \theta_m < 0 \\ s_s(\theta_m - \alpha_{sp}) & \theta_m \geq \alpha_{sp} \\ s_0 & 0 \leq r_{os}\theta_m < \varepsilon_1 \\ s_0 + \frac{\pi}{2}(r_{os}\theta_m - \varepsilon_1) & \varepsilon_1 \leq r_{os}\theta_m < \varepsilon_2 \\ s_0 + \frac{\pi}{2}(r_{os}\theta_m - \varepsilon_1) + \gamma(r_{os}\theta_m - \varepsilon_2) & \varepsilon_2 \leq r_{os}\theta_m < \varepsilon_3 \\ s_0 + \frac{\pi}{2}(\varepsilon_4 - r_{os}\theta_m) + \gamma(\varepsilon_4 - r_{os}\theta_m) & \varepsilon_3 \leq r_{os}\theta_m < \varepsilon_4 \\ s_0 + \frac{\pi}{2}(\varepsilon_5 - r_{os}\theta_m) & \varepsilon_4 \leq r_{os}\theta_m < \varepsilon_5 \\ s_0 & \varepsilon_5 \leq r_{os}\theta_m < \tau_s, \end{cases} \tag{3.36}$$

where α_{sp} is the stator slot arc, ε_1 is the arc length of half the tooth face, and

$$\begin{aligned} \varepsilon_2 &= \varepsilon_1 + h_0 \\ \varepsilon_3 &= \varepsilon_1 + h_0 + \left(\tfrac{b_0}{2} - h_0\right) \\ \varepsilon_4 &= \varepsilon_1 + h_0 + 2\left(\tfrac{b_0}{2} - h_0\right) \\ \varepsilon_5 &= \varepsilon_1 + 2h_0 + 2\left(\tfrac{b_0}{2} - h_0\right). \end{aligned} \tag{3.37}$$

To visualize (3.36), it is helpful to imagine a vertical line placed on the left side of Figure 3.3. As the arc length is increased azimuthally, the vertical line moves from the left to the right. Under the tooth face, the flux lines are assumed to be straight; therefore, the air gap is the nominal air gap. Once the vertical line reaches the slot opening, there is an additional length of flux path which is being approximated as a quarter circle. This is assumed to be the case until the vertical line is the length of h_0 away from the tooth due to the half circle representing a square area. From this point until $\tau/2$, there is a third component that is equal to the arc length described by γr, where r is the distance between the vertical line and the side of the tooth.

A similar expression is used to determine the effective air gap due to the rotor geometry. The effective air gap due to the rotor geometry can be defined as a repeating pattern of

$$s_r(\theta_m) = \begin{cases} s_r(\theta_m + \alpha_{rp}) & \theta_m < 0 \\ s_r(\theta_m - \alpha_{rp}) & \theta_m \geq \alpha_{rp} \\ 0 & 0 \leq \theta_m < \frac{\beta}{2} \\ \frac{\pi}{2} r_{ir}(\theta_m - \frac{\beta}{2}) & \frac{\beta}{2} \leq \theta_m < \frac{\pi}{2} \\ \frac{\pi}{2} r_{ir}(\pi - \frac{\beta}{2} - \theta_m) & \frac{\pi}{2} \leq \theta_m < \left(\pi - \frac{\beta}{2}\right) \\ 0 & \left(\pi - \frac{\beta}{2}\right) \leq \theta_m < \pi, \end{cases} \tag{3.38}$$

where α_{rp} is the rotor pole arc, β is defined as the ratio of the pole arc to the pole pitch, and r_{ir} is the rotor inner radius for an inside out machine.

The effective air gap is then calculated by combining the effective stator air gap with the effective rotor air gap. Here, it is important to note that the nominal air gap is shared; hence, the nominal air gap should only be included in one of the effective air gaps. In this derivation, it is included in the stator air gap, but it can alternately be included in the rotor air gap.

Depending on accuracy desired and the computational capacity, one or a combination of these approaches can be used to account for the geometry of the iron used in the machine.

3.2 Saturation

It is important to note that, up to this point, one major assumption is that the permeability of the materials is constant. This is a fairly limiting assumption, as it restricts the usefulness of the calculation of the flux density to the linear portion of the $B - H$ curve.

To account for saturation of the machine, it is useful to describe the conditions under which the machine will most likely experience saturation. In most cases, the machine can operate at the top of the linear range of the $B - H$ curve where it will not experience saturation significant enough to merit addressing. However, under extreme conditions, the controller of the machine could attempt to actuate the machine while it is operating close to the knee of the $B - H$ curve. During this actuation, the machine could, and likely would, experience saturation. Under these conditions, the saturation would most likely occur in the d-axis of the machine, shown as the direct axis in Figure

3.4. The direct axis of the machine is where the air gap is the narrowest. Air gap distance contributes to the opportunity for saturation. In most cases this would manifest as a saturation in the flare of the stator teeth under the pole faces of the rotor, the region between b_0 and b_1 in Figure 3.3. This will occur long before saturation becomes significant anywhere else in the machine.

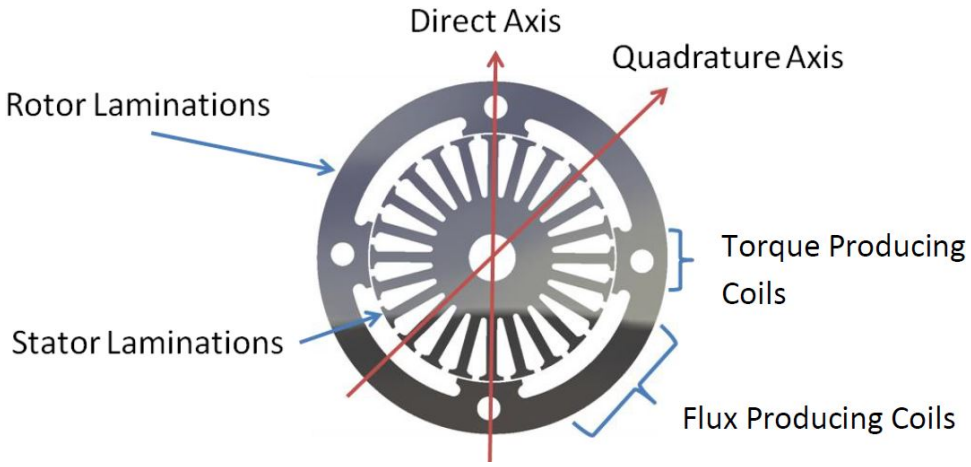

Figure 3.4: UIFESS drive bearing with direct and quadrature axis shown, from [2]

When saturation occurs, the permeability of the material approaches the permeability of air. With this in mind, it is helpful to define a virtual air gap where the virtual air gap is the effective air gap defined above plus the saturated iron. From [13], it is evident that the saturation of the machine occurs in the machine teeth, as the saturation creates a third harmonic flux component in the teeth. This can be considered the case when the machine is lightly saturated. However, when the machine is highly saturated, the core produces a third harmonic component directly opposing the third harmonic component produced by the saturation of the teeth. The analysis presented in this thesis will assume only light saturation. It is appropriate to assume the machine operation will not drive the machine into deep saturation because the quality of the machine operation will be greatly reduced under deep saturation.

The distinction between light saturation and deep saturation is expressed using various techniques and is not uniform across all applications. To distinguish these two types of saturation, it is convenient to define the level of saturation as an error between the linear projection of the ideal $B - H$ curve, L_{adu} in Figure 3.5, and the nonlinear $B - H$ curve, also shown in Figure 3.5. The point of transition between light and deep saturation is then defined as the point where the stator core of the machine is beginning to saturate. This point can be found using FEA software to determine the when the

stator core begins to saturate. This model uses a curve fitting approach to approximate the level of saturation.

The virtual air gap (s_v) is then described as [13]

$$s_v = \frac{1}{s_0^{-1} - k_m + k_m \cos(2(p\theta_m - \theta_f))}, \tag{3.39}$$

where

$$k_m = \frac{2}{3}\frac{k_{sat} - 1}{k_{sat} s_0}. \tag{3.40}$$

In this expression, s_0 is the nominal air gap, p is the number of pole pairs, θ_m is the angle measured around the air gap periphery, and θ_f is the position of the air gap flux with respect to phase q or a depending on the reference system chosen.

This representation involves a saturation factor (k_{sat}) that is determined using the saturation characteristics of the material, as shown in Figure 3.5. Using the method described in [14], k_{sat} can be approximated as

$$k_{sat} = \frac{\Psi_{at}}{\psi_{at} + \Psi_I}, \tag{3.41}$$

where

$$\Psi_I = \begin{cases} 0 & \Psi_{at} \leq \Psi_{T1} \\ A_{sat} e^{B_{sat}(\Psi_{at} - \Psi_{T1})} & \Psi_{T1} < \Psi_{at} \leq \Psi_{T2} \\ \psi_{G2} + L_{ratio}(\Psi_{at} - \Psi_{T2}) - \Psi_{at} & \Psi_{at} > \Psi_{T2} \end{cases} \tag{3.42}$$

and

$$\Psi_{at} = \sqrt{\Psi_{ad}^2 + \Psi_{aq}^2}. \tag{3.43}$$

In this expression, Ψ_{ad} and Ψ_{aq} are the $d-$axis and $q-$axis components of the air gap flux linkage. In per unit, Ψ_{at} is equal to the air gap voltage [14]. Also, A_{sat} and B_{sat} are used to fit an approximation function to the knee of the $B - H$ curve. This representation splits the saturation curve into three sections defined by the flux linkage magnitudes Ψ_{T1} and Ψ_{T2}. The flux linkage magnitude Ψ_{T1} is the point at which the saturation curve transitions from linear to nonlinear. The flux linkage magnitude Ψ_{T2} is the point where the saturation curve transitions from nonlinear to another linear region.

Since $\Psi = NBA$ and $MMF = Hl$, where N, A, and l are constants, this approach can be performed using the $B - H$ curve of the material for which saturation is being approximated. This transformation makes the calculation of k_{sat} simpler when using winding theory because the flux linkage does not need to be calculated. Instead, B is used to determine in which portion of (3.42) the system is operating. Also, the

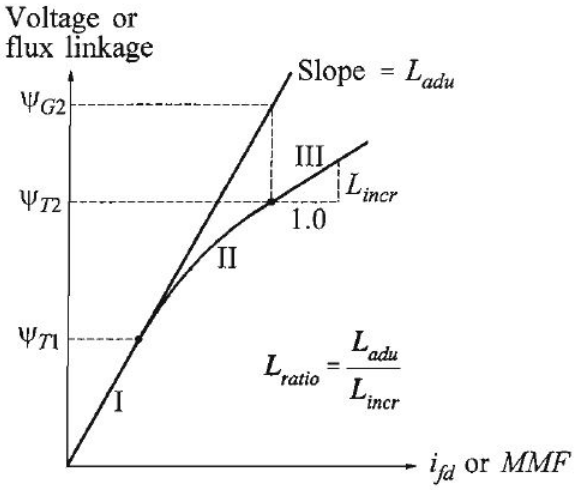

Figure 3.5: Representation of saturation characteristic, from [14]

inductance ratio is replaced by the ratio of the relative permeability to the incremental increase in B.

Development of a high speed FESS requires greater utilization of the available machine capability. This requires a more robust system design than that of the UIFESS due to the non-ideal effects of iron in the system. By incorporating the effects of iron and saturation into the machine air gap the overall model accuracy is improved. This allows for improved machine design and more robust control system development.

Chapter 4

Dynamic Modeling

Previous models of the UIFESS focused on the bearing aspects of the machine [2]. The project has need of a model that could predict torque production and dynamically respond to both changes in position and current distribution. This model needs to be capable of determining the effects of non-ideal materials being used in the rotor. It is also advantageous for the model to predict the losses due to saturation and the effects of mechanical deformation of the rotor.

The model developed in [2] is capable of dynamic response in terms of radial forces. However, that model was developed using many ideal assumptions regarding materials and the air gap. The model developed in this thesis is an extension of the model developed in [2] to improve the accuracy of the UIFESS model and provide the capability to predict torque. To improve the accuracy of the model, the work of the last two chapters is incorporated into the modified winding theory discussed in [2]. The inclusion of torque production is discussed below and relies heavily on modified winding theory.

Although the model in this thesis relies on the work presented in [2], it is important to point out that the values presented in [2] for the machine turns function were not used due to an error in the calculation. The method used produces values, that compared to FEA results, have low error for force production, but there appears to be a typographical error in the implementation, resulting in an incorrect number to negative windings. Also, the turns per coil for the turns function in [2] was defined as the number of turns per coil. This is inaccurate for the machine architecture because each slot houses two coils in the UIFESS.

4.1 Torque Production

Torque is produced during two phases of the machine's operation, motoring and generating. Motoring torque is generated when the electrical angle of the machine is advanced in relation to the mechanical angle of the machine. Generating torque is produced when the electrical angle is retarded in relation to the mechanical angle of the machine. The torque production is modeled by calculating the derivative of the air gap energy, or magnetic co-energy, as a result of a mechanical or electrical change of position with respect to the displacement angle.

To better understand the torque produced by the machine, it is useful to first consider a degenerate form of the generating case. In this case, the machine is energized with a particular current profile. This current profile produces a MMF that is in alignment with the rotor position, creating a minimum energy condition. Then, an external force changes the angle of the rotor by a small amount. This changes the MMF distribution of the rotor due to the change in the air gap. This change in MMF changes the energy stored in the air gap. This results in a restoring torque on the rotor that is attempting to return the rotor to the position of minimum energy.

The energy can be expressed as the energy density of the magnetic field integrated over the volume of the magnetic field [19] as

$$W = \int_V \left(\int H \cdot dB \right) dV. \tag{4.1}$$

Using the triple integral for volume of a circular cylinder in cylindrical coordinates, (4.1) can be applied to the air gap to obtain

$$W = \int_0^{2\pi} \int_{r_s}^{r_s+s(\theta)} \int_0^h \left[\int H \cdot dB \right] dl r dr d\theta, \tag{4.2}$$

where the triple integral is defining the air gap of the machine in terms of the machine height (h), the stator radius (r_s), the air gap ($s(\theta)$), and the azimuthal angle from 0 to 2π.

Assuming materials with constant permeability, this simplifies to [19]

$$W = \int_0^{2\pi} \int_{r_s}^{r_s+s(\theta)} \int_0^h \left[\frac{B^2}{2\mu_0} \right] dl r dr d\theta. \tag{4.3}$$

From the modified winding function, it is clear that B is varying azimuthally; however, it is appropriate to assume that the magnetic flux density is not varying within the air gap axially or radially. This results in the further simplification of (4.3) to

$$W = \int_0^{2\pi} \left(\left[\frac{hB(\theta)^2}{2\mu_0} \right] \frac{(r_s + s(\theta))^2}{2} - \left[\frac{hB(\theta)^2}{2\mu_0} \right] \frac{(r_s)^2}{2} \right) d\theta, \tag{4.4}$$

which through expansion of terms reduces to

$$W = \int_0^{2\pi} \left(\left[\frac{hB(\theta)^2}{2\mu_0} \right] \frac{(2r_s s(\theta))}{2} + \left[\frac{hB(\theta)^2}{2\mu_0} \right] \frac{(s(\theta))^2}{2} \right) d\theta. \tag{4.5}$$

Then, by combining (4.5) with $B = \mu_0 \mu_r H$, where $\mu_r = 1$ because the only material in the air gap is air, and pulling the constants out of the integration becomes

$$W = \frac{h\mu_0}{4} \int_0^{2\pi} \left((2r_s) H(\theta)^2 s(\theta) + H(\theta)^2 s(\theta)^2 \right) d\theta. \tag{4.6}$$

Finally, an equation to solve for air gap energy with respect to a change in rotor angle (ϕ) can be defined as

$$W(\phi) = \frac{h\mu_0}{4} \left[\int_0^{2\pi} 2r_s \frac{\mathcal{F}(\theta)^2}{s(\theta, \phi)} d\theta + \int_0^{2\pi} \mathcal{F}(\theta)^2 d\theta \right], \tag{4.7}$$

where $\mathcal{F}(\theta)$ is the MMF at θ and is calculated using (2.23), and $s(\theta, \phi)$ is the air gap shifted by ϕ.

There is a lot of information packed into this expression of the air gap energy. First, this calculation requires the computation of the total MMF in the machine air gap. This can result in very slow computation times due to the integration. Also, as the rotor angle changes the MMF distribution changes requiring the recalculation of the MMF with respect to the new air gap.

Once the W is calculated, the torque can be found by taking the derivative of W with respect to the change in the angle of the machine as

$$\tau = -\frac{dW}{d\theta}. \tag{4.8}$$

In (4.8), the angle θ is either mechanical or electrical depending on the operational state of the machine. In this expression of torque, the calculation of the energy in the air gap is changing due to motoring or generating conditions. Motoring torque is found by keeping the rotor in place and determining the new MMF distribution caused by the current distribution being advanced by θ_e. Due to the physical layout of the machine, W_{θ_e} is discontinuous, as θ_e has discrete values. Generating torque is found by keeping the current distribution fixed and moving the rotor to θ_m. In other words, shifting the air gap by θ_m, since a change in the rotor position is reflected in the air gap.

This is not the only method of determining the machine torque, but it is sufficient for this stage of the machine modeling and serves as a validation tool for future generations of the machine model. Another approach is to compute the inductance matrix $[L(\theta)]$ of the machine and use that matrix to determine the electromagnetic torque as [20]

$$\tau = \frac{1}{2} [i_s]^T \left[\frac{\partial [L(\theta)]}{\partial \theta} \right] [i_s], \tag{4.9}$$

where $[i_s]$ is the stator current matrix represented in a *abc* or *dqn* axis reference.

The torque production can also be determined for non-ideal materials and iron by incorporating the concepts developed in the previous two chapters.

To develop a dynamic torque model, the energy is defined as a function of current, air gap, and position using (4.7), (2.23), and the effective gap. Then, the torque is found from the energy stored in the air gap. The torque will produce an acceleration of the rotor which will affect the position. Then, the energy is updated, and the process begins again.

This iterative approach is very computationally expensive due to the large number of integrations involved. Also, due to the consecutive nature of the problem, the equations cannot be run in parallel to increase performance.

4.2 Material Effects

In order to allow the model to account for the materials used in the machine, two effects need to be incorporated. The first is the effect of non-ideal materials used for the rotor. The second is the effect of the long path lengths of iron relative to the air gap length. Accounting for these effects is important when attempting to develop a conservative model that is then used for an iterative design process.

The effect of using composite materials in the rotor of the machine is modeled using the composite loss factor. Due to the relatively simple geometry of the stabilization bearing, the composite loss factor used is the k_{com}, developed in (2.9). However, for the drive bearing, the more complex k_{com}, developed in (2.28), is used to account for the length of material under the pole face in the MMF calculation.

To determine the effective air gap, the method presented in (3.36) and (3.38) is used, and the rotor geometry is assumed to have uniform pole thickness. This is not an entirely accurate representation of the rotor geometry, but it is a close approximation.

4.3 Saturation

Saturation is not included in simulations based on the models derived in this thesis due to time constraints. The effect of saturation is incorporated for a machine with an iron rotor or a machine with a composite rotor. This effect is represented as an effective increase in the air gap due to the saturation of the stator and modeled using (3.39) through (3.43), where s_0 is equal to the effective air gap. The key difference between the iron rotor and the composite rotor is that a composite rotor causes the machine stator to saturate at a higher current due to the reduced flux density.

4.4 Mechanical Dynamics

A portion of the mechanical dynamics of the machine is described in [2], which include rotor translation and tilt. Rotational dynamics are described in section 4.1. Radial dynamics are another important set of dynamics that should be considered when discussing a high speed FESS. These dynamics are discussed in [5] and [6].

The primary concern, from the perspective of controlling the machine, when considering high speed rotation is radial deformation of the rotor. This is modeled with an ideal representation, uniform deformation, or non-ideal representation, non-uniform deformation. For the ideal case, the deformation (u_r) can be described as [5]

$$u_r = \frac{3+v}{8}\rho\omega^2\frac{1-v}{E}r\left[a^2+b^2-\frac{1+v}{3+v}r^2+\frac{1+v}{1-v}\frac{a^2b^2}{r^2}\right], \tag{4.10}$$

where v is Poisson's ratio, ρ is material density, ω is rotational velocity, E is elastic modulus, a is inner radius, and b is outer radius. This equation for deformation is assuming a cylinder of uniform thickness and should be considered a lower bound for the deformation.

A more accurate model of radial deformation can be developed using surrogate modeling techniques in conjunction with FEM. This process, using ordinary Kriging as a surrogate model, is described in [5].

It should also be noted that the dynamics presented in [2] are assuming that the rotor is a rigid body. This assumption will not be valid if the rotor deflects radially. Non-rigid modeling is very complex and tends to be very computationally expensive.

4.5 Model Development

The model of the UIFESS is intended to be used as a design tool to explore the effects of various design decisions aimed at developing a high speed FESS. The model is intended to be used in conjunction with a control system model to test control schemes developed for the machine. Therefore, the model needs to be capable of representing the system dynamics. This indicates a model that is modular in the sense that components can be interchanged without redevelopment of the model. In order to meet these goals, a MATLAB® model is desired to interface with the control systems that is developed using MATLAB® or Simulink®.

To develop a modular model, the system is designed as a collection of components. Each component is defined as the physical properties of that component, such as geometry, mechanical streaming, and permeability. Then, the interactions are defined by

the component properties; this allows the model to recalculate the interactions when new system perimeters are specified. For example, if the rotor geometry changes, it will change the air gap of the machine. Because the forces and torques are functions of the air gap, these interactions are updated to reflect the new geometry. The model is composed of several files that are called by a main file to compute the dynamics of the system. These files are located in the Appendix.

This model primarily focuses on the torque production of the drive bearing. This includes the definition of the initial coil currents, the stator geometry, and the rotor geometry. Then, the model is able to calculate:

- the effective air gap using (3.35) - (3.38)
- the turns function as defined in [2]
- the modified winding function using (2.24) with the air gap replaced by the effective air gap
- the air gap MMF using (2.23) and flux density $B(\theta)$ by multiplying the MMF by the effective air gap and μ_0
- the energy using (4.7), and
- the torque using (4.8).

A model developed in this fashion involves a large number of definitions and calculations. This results in many points of failure due to inaccurate interaction definitions or typographical errors. Therefore, it is crucial to verify the model results.

Chapter 5

Results and Verification

To determine the applicability of the models to the UIFESS, the models need to be verified and validated. Verification of the models is accomplished with the aid of finite element analysis (FEA). Validation of the models requires an operable machine and is, therefore, left as a future exercise for the UIFESS group.

5.1 Effects of Composite Materials

The model verification is performed using a finite element analysis program called Finite Element Method Magnetics (FEMM), a freeware program [21]. The first model produced in FEMM, shown in Figure 5.1, represents the demonstrator used by the UIFESS team to test single axis control schemes, shown in Figure 5.2. This FEMM model was intended to verify the values of B predicted by the analytical approach and magnetic circuit approach. This model was also intended to verify the effects of composite materials on the B field produced by the electromagnet. The demonstrator and the model configuration perimeters are listed in Table 5.1. In this section, the terms iron and M36 steel are considered to be interchangeable, as the machine is composed of M36 steel.

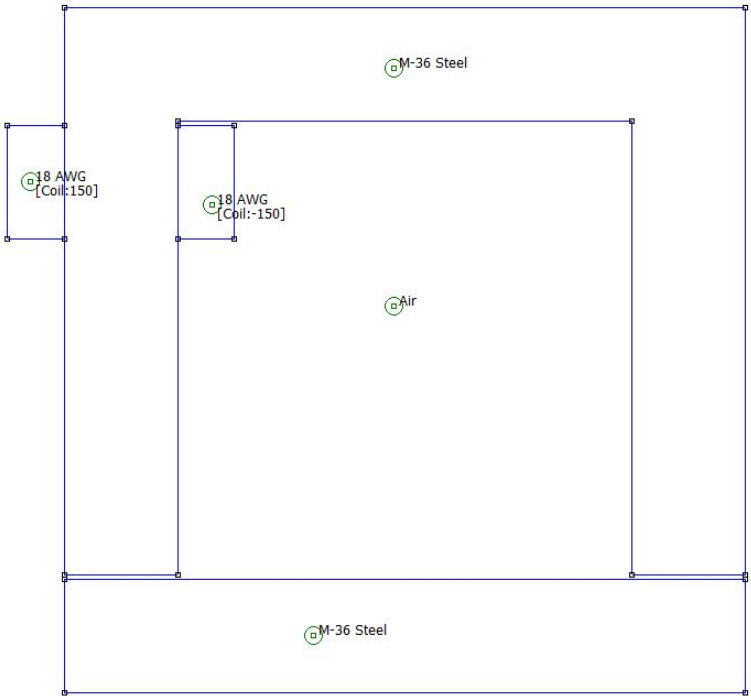

Figure 5.1: FEMM model of the UIFESS demonstrator

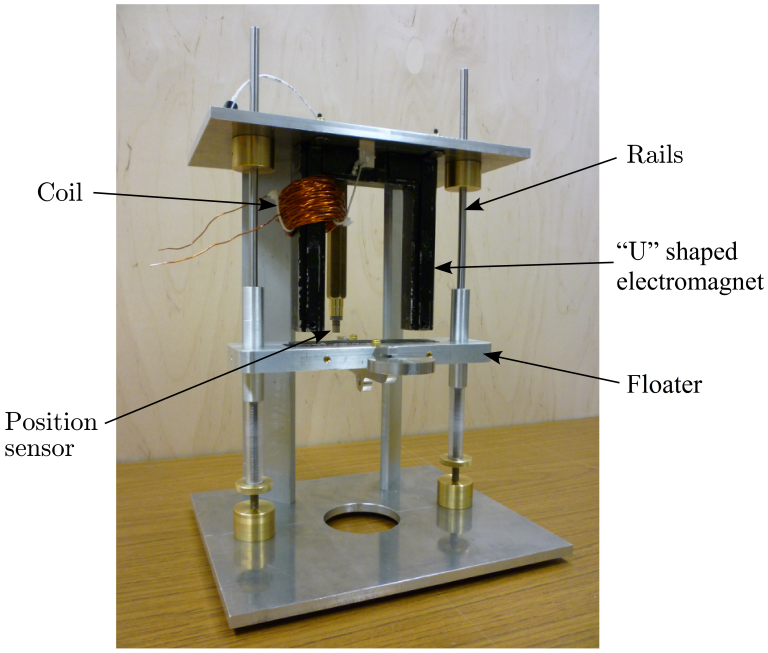

Figure 5.2: UIFESS single axis electromagnet demonstration device, from [3]

To determine the effect of a composite floater, the model is ran twice. The first simulation is ran with the floater material set to iron. The second simulation is ran

Table 5.1: Model parameters based on demonstrator

Parameter	Value
Number of turns	150
Bias current	1.91 A
Material	M-36 Steal
Material relative permeability	1616
Nominal air gap	1 mm
Cross sectional area	645.16 mm^2
Floater length	152.4 mm
Horse Shoe length	482.6 mm
k_{com}	0.312

with the floater material set to a composite. The composite used for these verification results is described in [5], and it has a relative permeability of 30. This composite is approximately 70% iron by volume and is not realistic under the method used to develop the composites tested in [5] due to its low yield strength. It could be manufactured with favorable mechanical properties using other techniques described in [5].

The FEMM results of the simulation with the floater composed of iron are shown in Figure 5.3 (a). The simulation results are consistent with expectations of small values for leakage, fringing, and cornering with respect to the field contained within the material. The FEMM results of the simulation with the floater composed of an iron composite are shown in Figure 5.3 (b). The simulation results show more significant leakage than the case when the floater is composed of iron and what could be considered extreme fringing. The fringing reaches a point that the field is passing through the air between the poles rather than entering the floater.

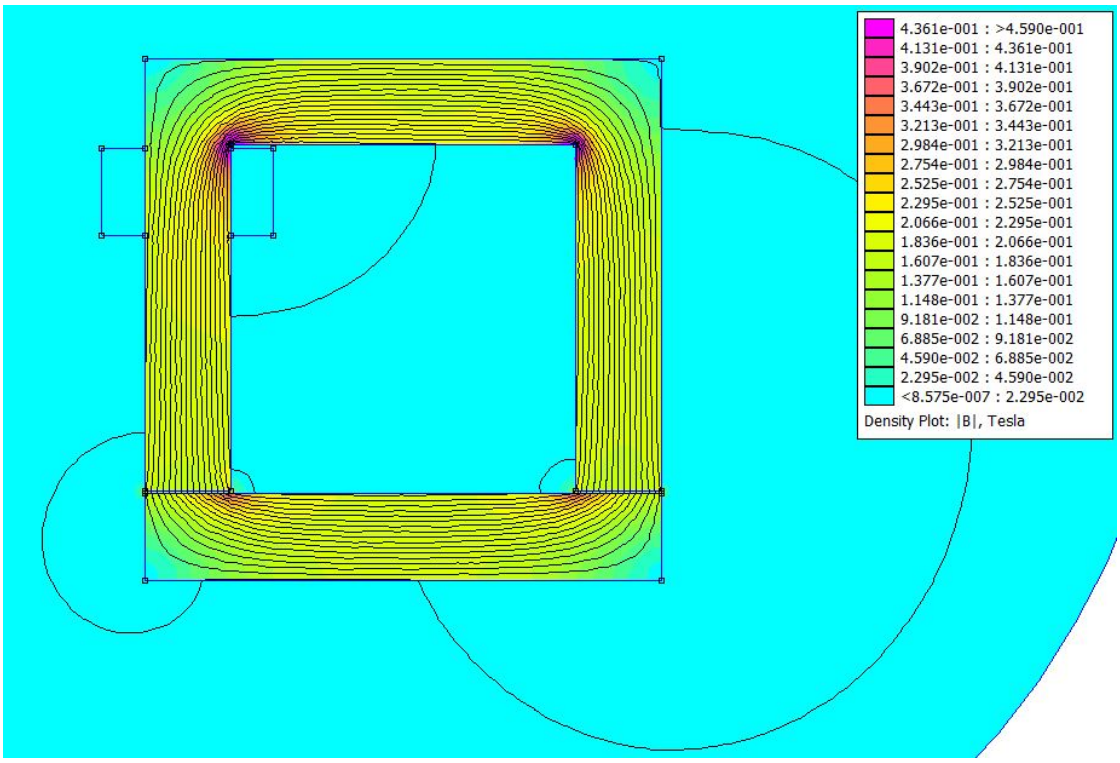

(a)

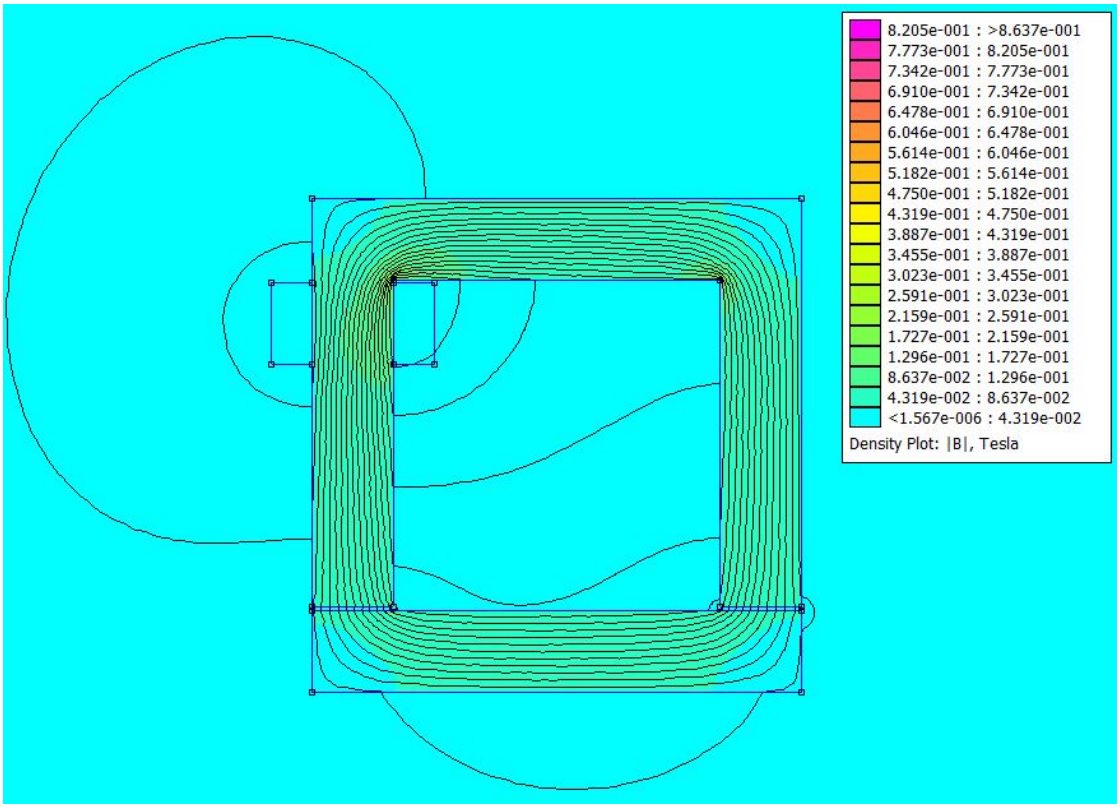

(b)

Figure 5.3: FEMM results of demonstrator with (a) iron floater and (b) composite floater

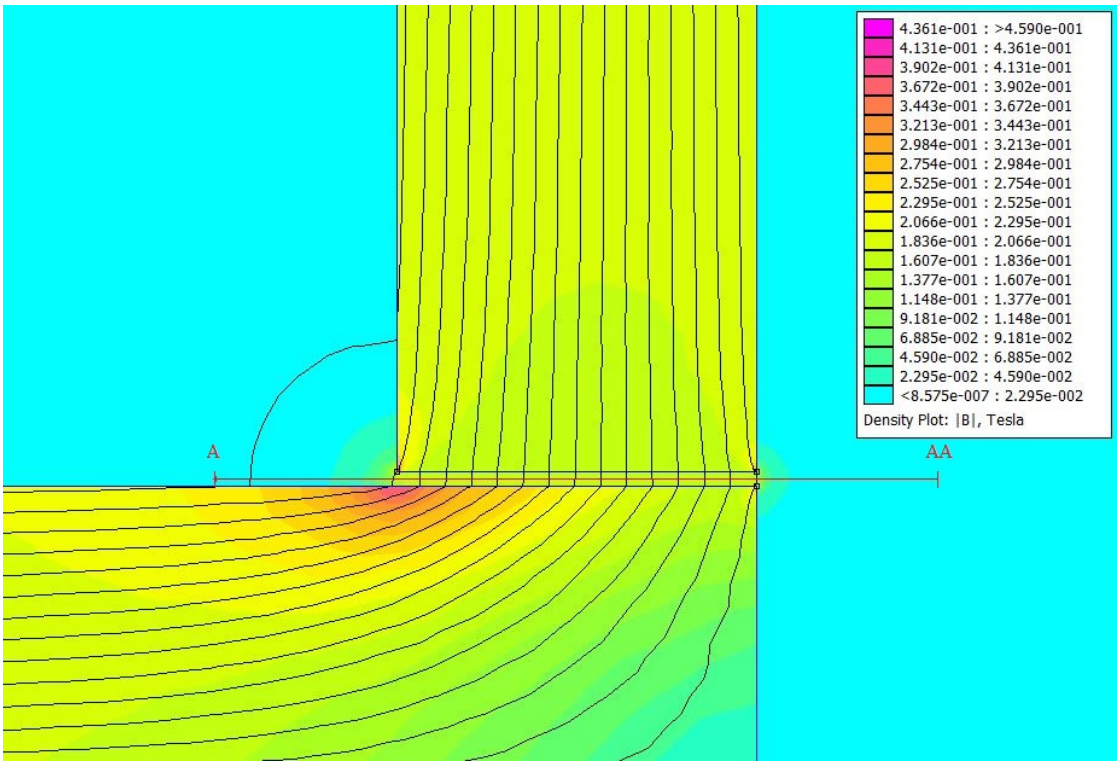

(a)

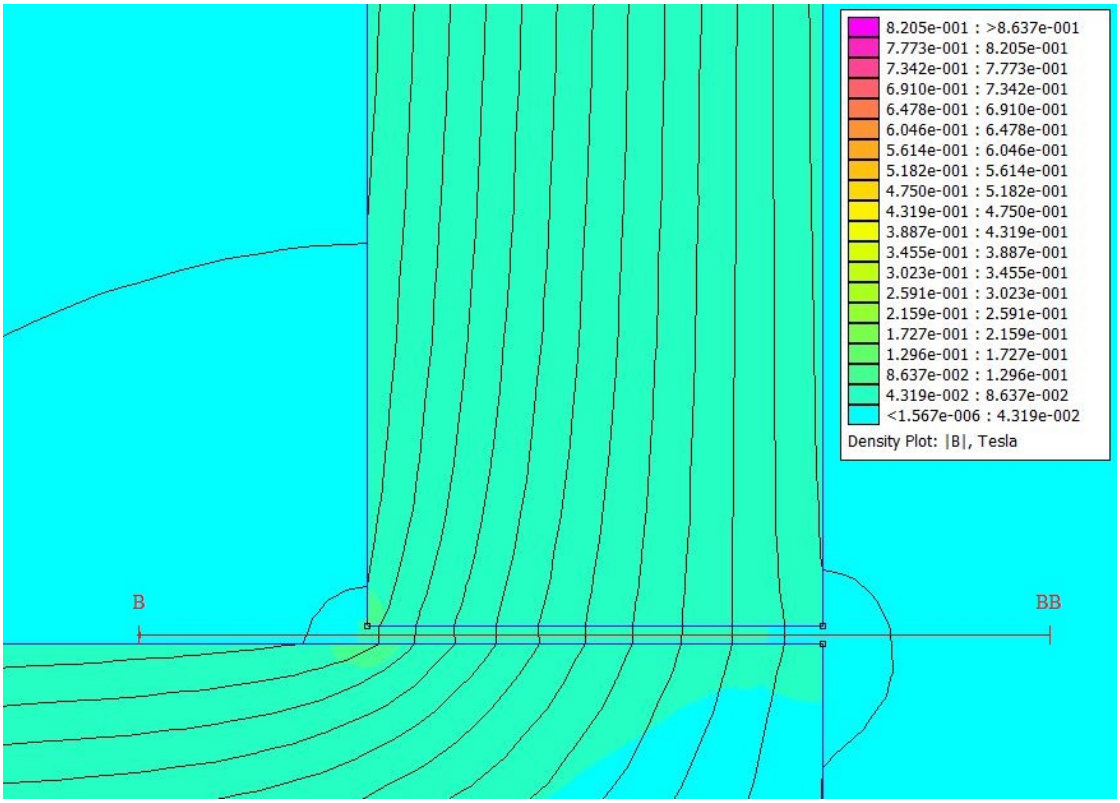

(b)

Figure 5.4: FEMM B across air gap for (a) iron floater and (b) composite floater

The lines shown in Figure 5.4 are used to sample the value of B for both (a) an iron floater (A-AA) and (b) a composite floater (B-BB). The values sampled are plotted versus the length along the line, shown in Figure 5.5. These lines were defined by the end points (5.5, 2.02), for A and B, and (7.5, 2.02), for AA and BB, in both cases to ensure that the flux density could be compared.

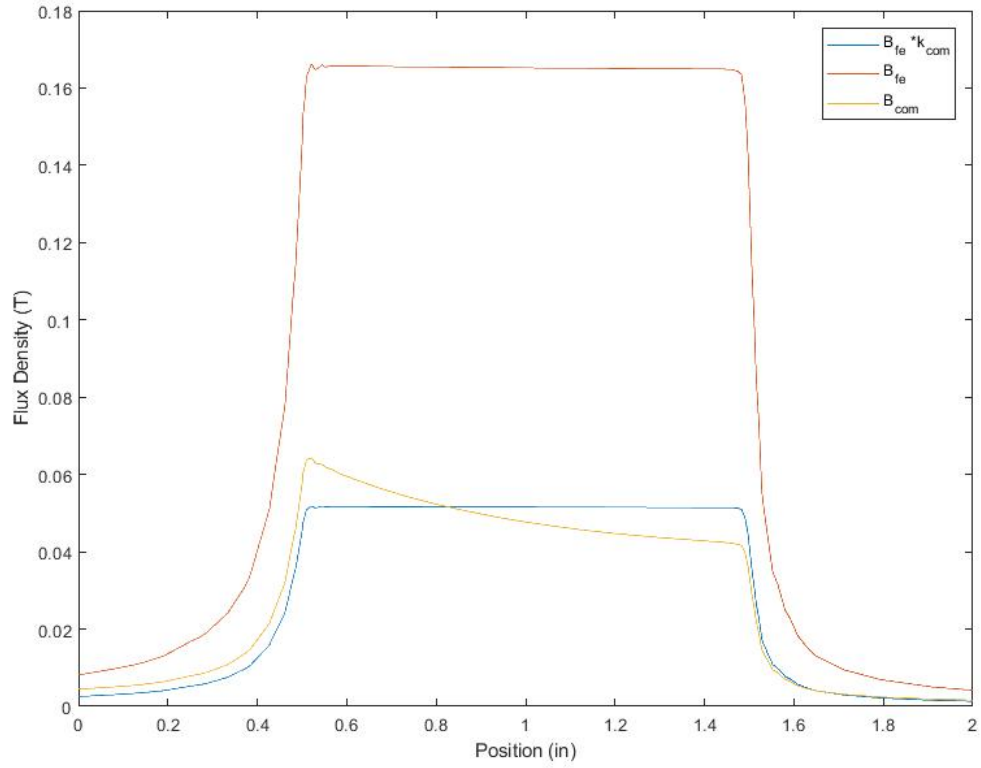

Figure 5.5: FEMM results for flux density under the pole face of the demonstrator

An important observation from Figure 5.5 is the shape of B_{fe}, from Figure 5.4 (a) (A-AA), and B_{com}, from Figure 5.4 (b) (B-BB). The flux density under the pole face with an iron floater has little deviation, but the flux density under the pole face with a composite floater has a variation of about 35% from left to right. This can cause significant error at the edges of the pole face when using the composite loss factor.

The analytical and equivalent circuit models assume the value of B is constant within the surface area used. To compare the models with the FEMM results, a point is chosen at the middle of each line, (A-AA) for the iron floater and (B-BB) for the composite rotor, shown in Figure 5.4. The values from FEMM are then compared to the values predicted by the models, represented in Table 5.2.

Table 5.2: Comparison of methods used to calculate B in Tesla

Method Used	B_{fe}	B_{com}	$B_{fe} * k_{com}$
Analytical	0.157	0.049	0.049
Equivalent Circuit	0.150	0.046	0.047
FEMM	0.166	0.048	0.052

The percent difference is then calculated between each modeling approach and the FEMM results, presented in Table 5.3. The error of the analytical method is very low while the error of the equivalent circuit method is higher than expected. The equivalent circuit model could be improved by including the leakage and fringing effects; however, this approach will not provide the same variation in the flux density under the pole face. The added complexity and computational overhead involved in improving the prediction of the equivalent circuit approach is ultimately not worth the gain in improvement. Also, the analytical method has a sufficiently low error and represents the lower bound of the FEMM results, making it a conservative estimate.

Table 5.3: Comparison of method error against FEMM

Method Used	B_{fe}	B_{com}	$B_{fe} * k_{com}$
Analytical Error	5.76%	1.65%	1.65%
Equivalent Circuit Error	5.76%	4.82%	2.35%

Another verification step is to ensure that the relationship between force and flux density is maintained while using the composite loss factor. For this relationship to be maintained, the force acting on the floater needs to be proportional to k_{com}^2. FEMM results indicate a force of 14.96 on the iron floater and a force of 1.47 on the composite floater. This represents an error of 0.86% when using k_{com} between the FEMM composite force and the FEMM iron force times k_{com}^2.

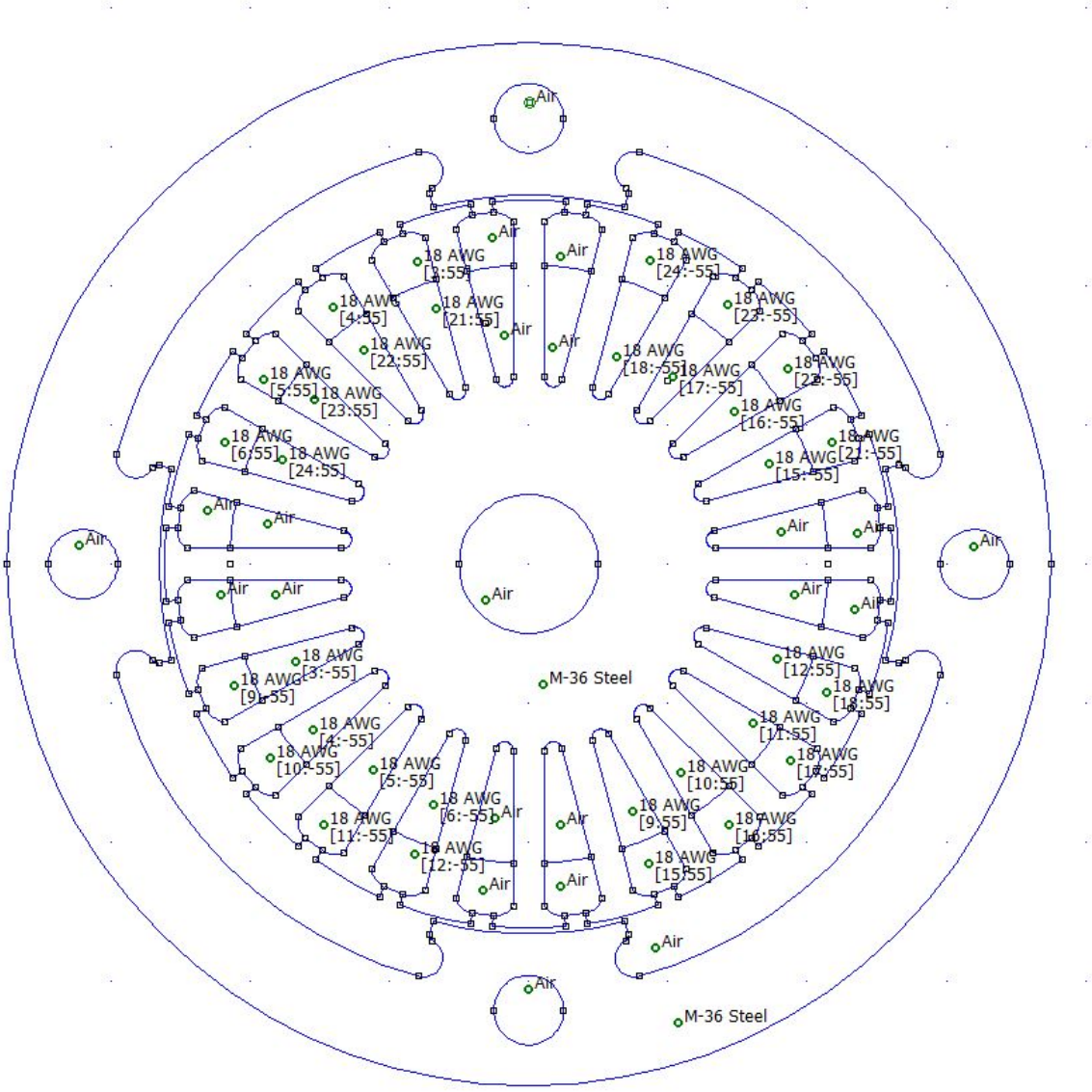

Figure 5.6: FEMM model of the drive bearing using the current machine geometry

The second model used in FEMM is of the drive bearing, shown in Figure 5.6. This model is the same as the one used in [2] with only the d-axis active. As seen in Figure 5.7 (b), the composite rotor results in lower saturation and more fringing when compared to the iron rotor shown in 5.7 (a). The results for the machine geometry are in agreement with the results of the demonstrator.

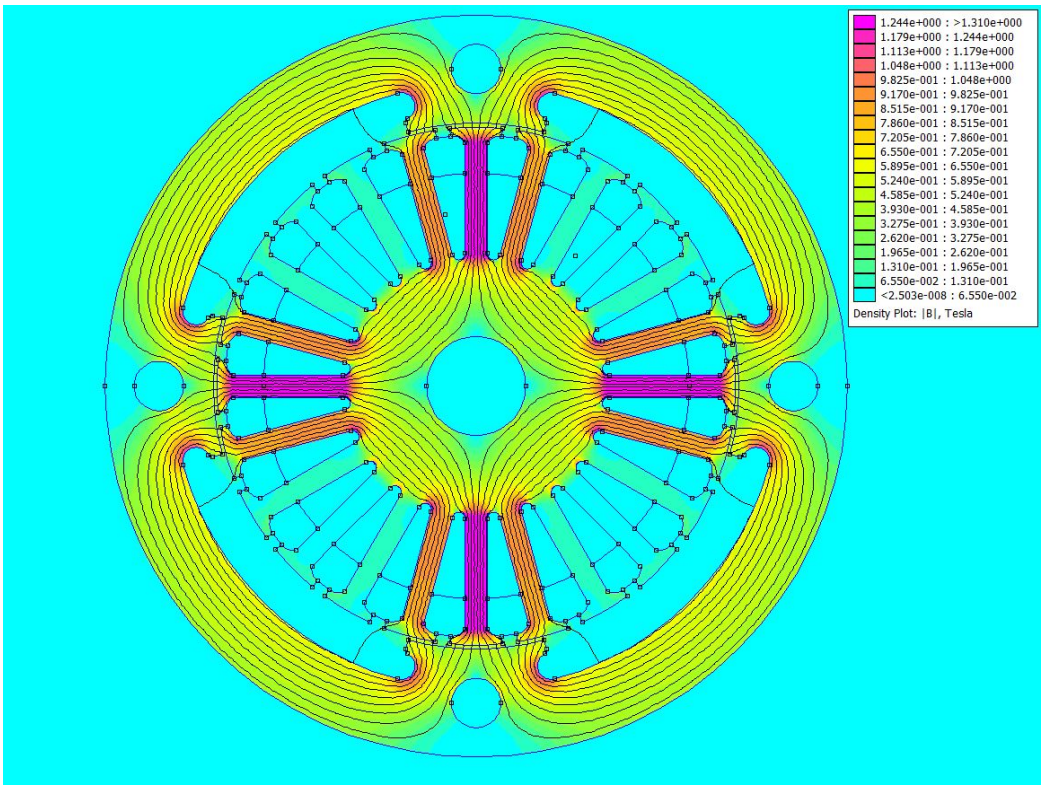

(a)

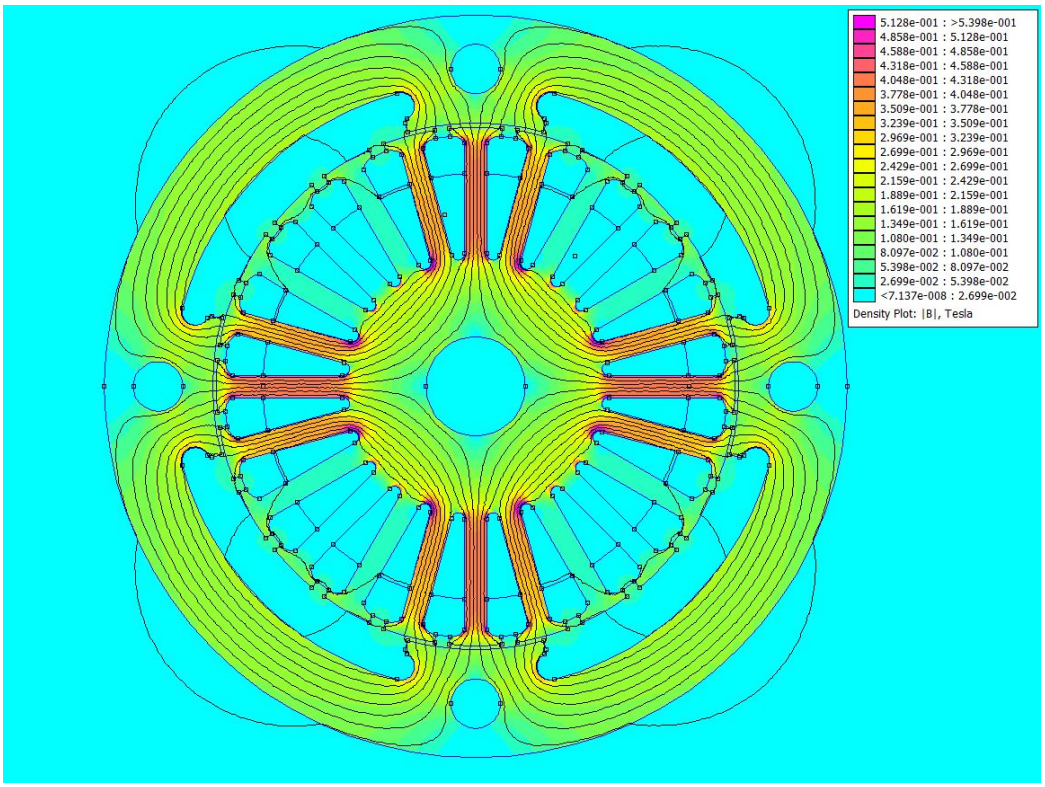

(b)

Figure 5.7: FEMM results for the drive bearing with (a) an iron rotor and (b) a composite rotor

Once again, the flux density was plotted as a function of the distance along the arc paths shown in Figure 5.8 (a) (A'-AA') and (b) (B'-BB'); these arc paths were defined by a line from (2.46, 1) to (2.46, -1) and an arc of 42°.

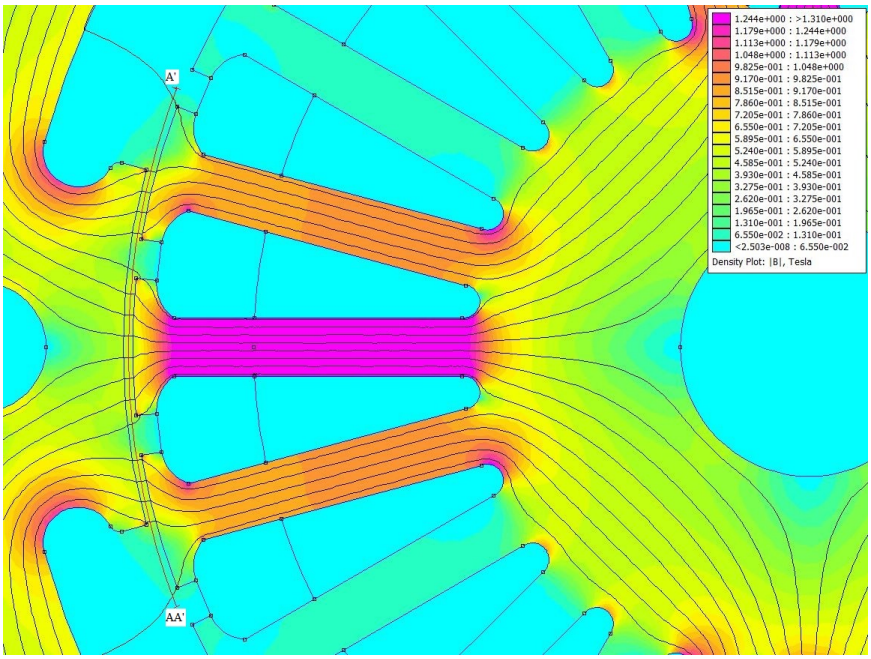

(a)

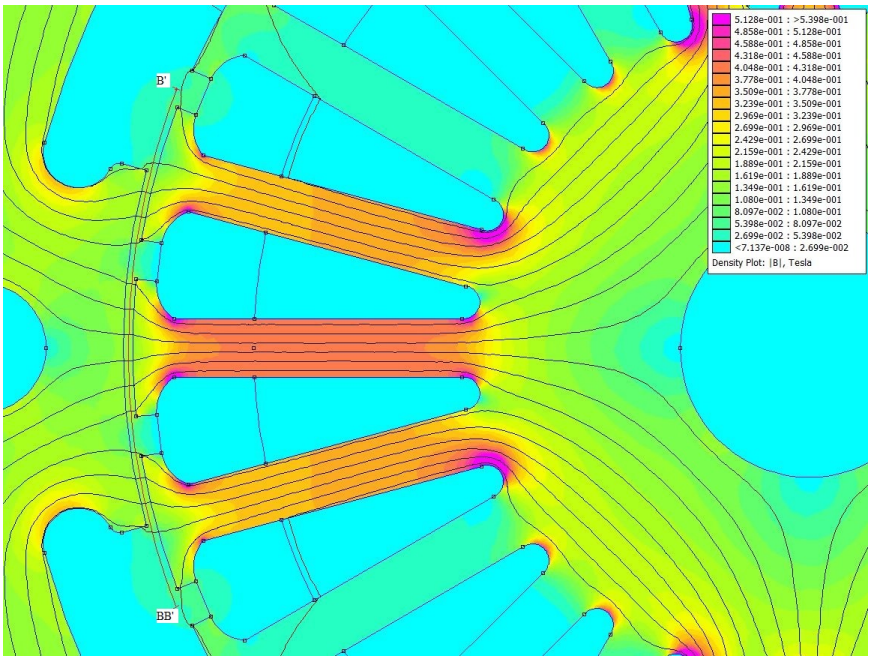

(b)

Figure 5.8: FEMM B across air gap for (a) iron rotor and (b) composite rotor

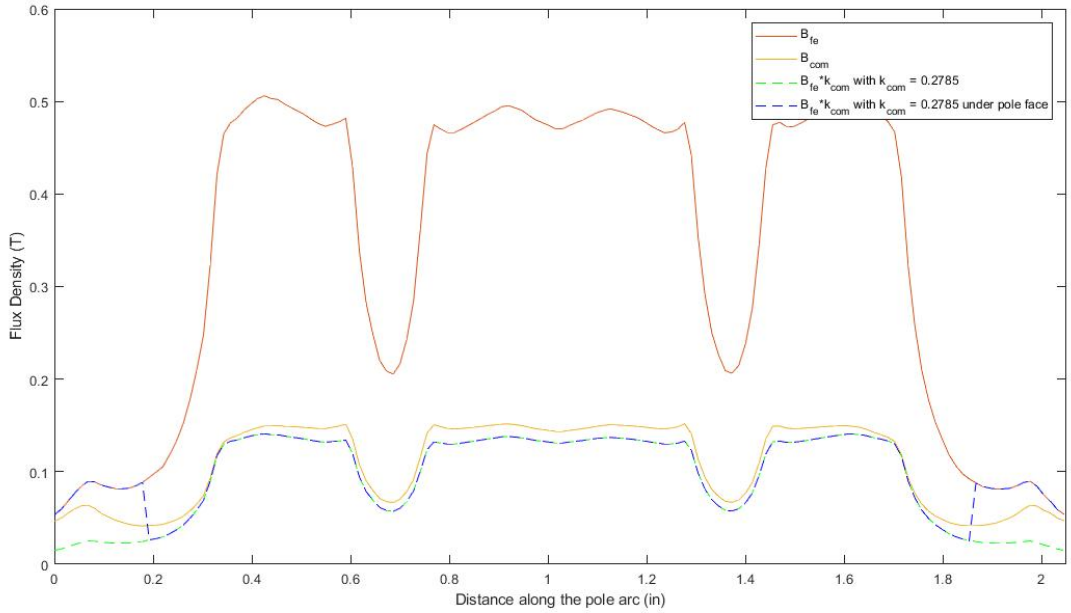

Figure 5.9: FEMM results for flux density under the pole face of the rotor

The results of Figure 5.8 and the incorporation of the composite loss factor are plotted in Figure 5.9 as a function of the position along the arc under the pole face. There are a few important observations to be made from Figure 5.9. The first is that (2.27) does not accurately predict the flux density in the interpole region when a composite material is used in the rotor. This makes intuitive sense because the flux is not exiting the rotor in the interpole region, so the dominant effect on the flux density is caused by the air gap.

To observe the impact of a constant composite loss factor, k_{com} is defined using (2.9). To account for the different portions of the stator, l_{fe} is defined as two times the stator slot depth plus the arc length through the stator core between two poles of the rotor. Then, l_c is defined as two times the pole depth to the center of the rotor plus the arc length between two poles of the rotor: as a result, k_{com} equals 0.28. This causes the error of $B_{fe} * k_{com}$ in the air gap at the boundary to be quite high, which is true for all fixed values of k_{com}. To correct for this observation, (2.27) is modified to only affect B under the pole face resulting in (2.28).

The final observation is that the flux density present in an iron rotor scaled by the composite loss factor is a lower bound of the actual flux density that appears in the composite rotor. This indicates that the use of k_{com} produces a conservative estimate, and when using (2.28), this estimate has an error of about 11.15% in the center of the

rotor. The error between the $B_{fe} * k_{com}$ and B_{com} has a mean value of 19.64% due to the large difference between the values of $B_{fe} * k_{com}$ and B_{com} near the edge of the pole.

The final verification step for the composite effects is to run the FEMM model with both d-axis and q-axes active. Then, compare the results to the predictions found using the modified winding theory described in [2]. The results of the two methods are consistent with the expectations developed from the d-axis only results.

There are two noteworthy observations to be made from Figures 5.10 and 5.11 that need to be addressed. The flux density distribution predicted by the modified winding function is not accurate when compared to the FEMM results. The largest errors are at the edges of the rotor poles. The difference between the two models at the entering edge is equivalent to the difference between the two models at the departing edge.

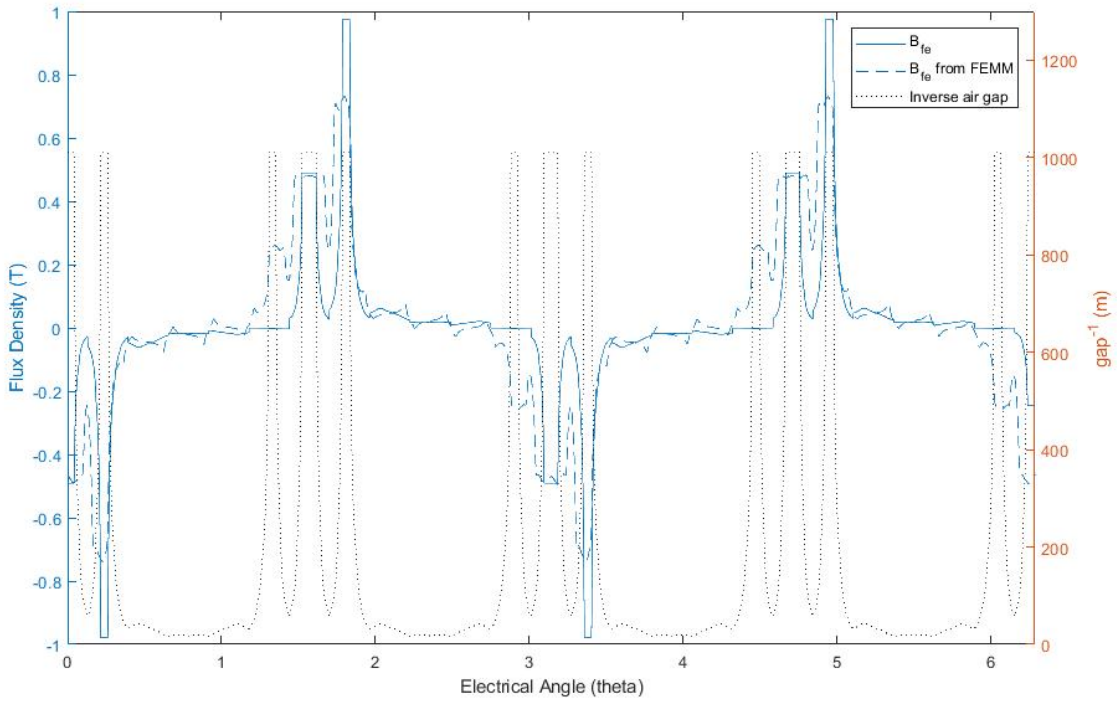

Figure 5.10: Flux density in the air gap of the drive bearing using the current machine geometry with an iron rotor

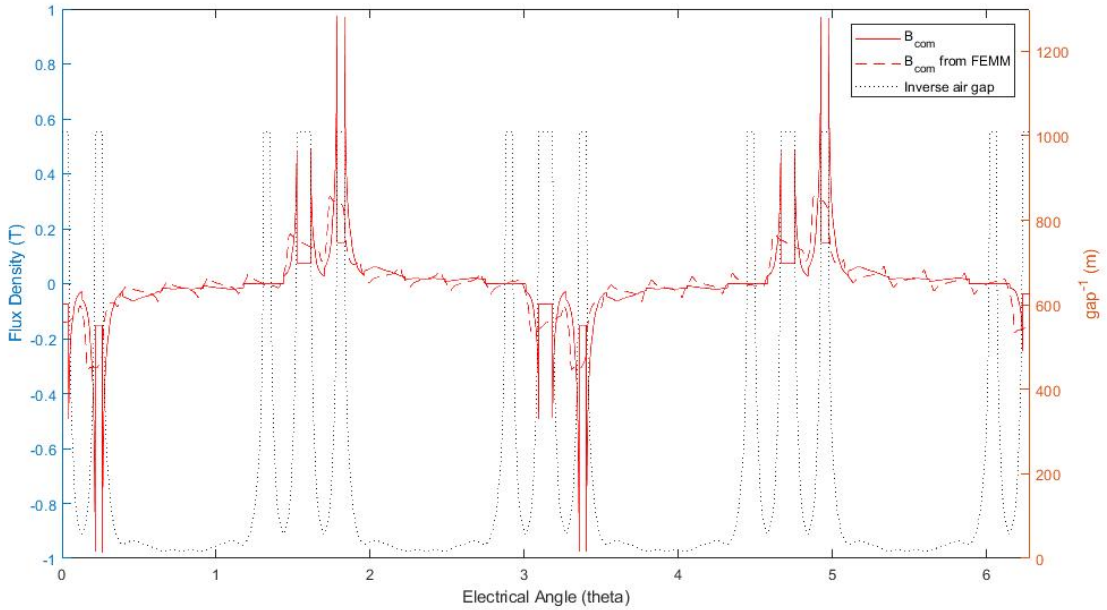

Figure 5.11: Flux density in the air gap of the drive bearing using the current machine geometry with a composite rotor

The model predicts the MMF of the machine then scales the MMF by the air gap and the permeability of air to calculate the flux density. The MMF is calculated using the coil currents and the modified winding function. The modified winding function is defined by the turns function and the inverse air gap. As the air gap appears to be sufficiently defined, the most likely cause of the error is the definition of the turns function used in the model.

Also, there is error associated with the effective air gap. This could be a result of measurement error in the dimensions of the stator teeth or an overly conservative approximation of the effective air gap. A less conservative approximation of the effective air gap can improve these results. For this particular rotor configuration if the stator slot opening and stator top slot width are reduced to half the value given in [2], the approximation is much closer to the FEMM results. The actual rotor geometry should be verified before modifying the approximation.

The composite loss factor can be improved using FEMM results once the composite material is chosen and the permeability of the composite is known. For the composite discussed in [5], the composite loss factor calculated was about half the value indicated by FEMM. The calculated k_{com} is about 0.15, but the value indicated by FEMM is around 0.30, shown in Figure 5.12. It is possible that this is due to k_{com} being calculated using the path defined by one pole set. Further FEMM testing should be done to determine

if this relationship holds for various values of the composite permeability and rotor configurations.

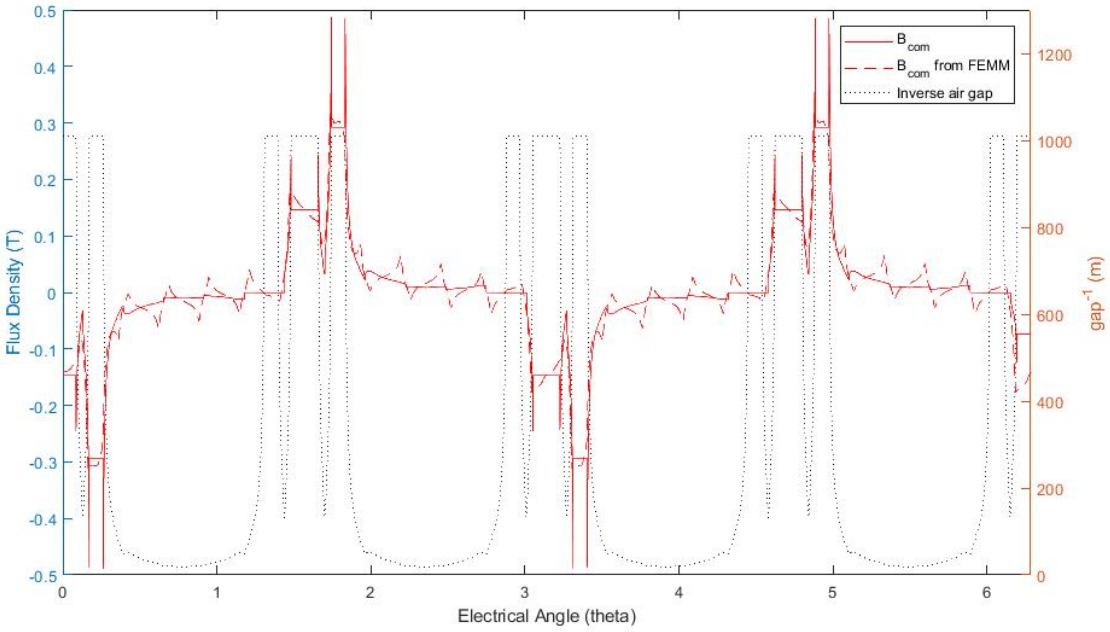

Figure 5.12: Flux density in the air gap of the drive bearing using the current machine geometry with a composite rotor and k_{com} fit using FEMM data

5.2 Torque Production Simulation

The torque production results found using the air gap energy are presented in Figure 5.13 for the UIFESS with an iron rotor. The torque production results for the UIFESS with a composite rotor with a k_{com} of about 0.15 are presented in Figure 5.14. In Figures 5.13 and 5.14, the negative torques are indicating a torque in the clockwise direction. Also, the torque is calculated using (4.8) to find the incremental torque due to each change of the position of the q-axis. Then, the incremental torques are summed to find the resultant torque. The discrete nature of the torque is due to the discrete angles that the q-axis are placed, since the q-axis can not be placed arbitrarily between the stator teeth.

These results make intuitive sense. As the electrical angle is advanced in the clockwise direction, the rotor will experience a force pulling it toward the q-axis. At 45°, the q-axis will be acting on both of the poles of the rotor resulting in a lower torque magnitude in the clockwise direction. When the angle is advanced beyond 60°, the dominant interaction is due to the next rotor pole in the machine. This will cause the

sign to invert, and the rotor will be pulled in a counter clockwise direction. Once the q-axis reaches 90°, the torque is zero and the pattern will repeat.

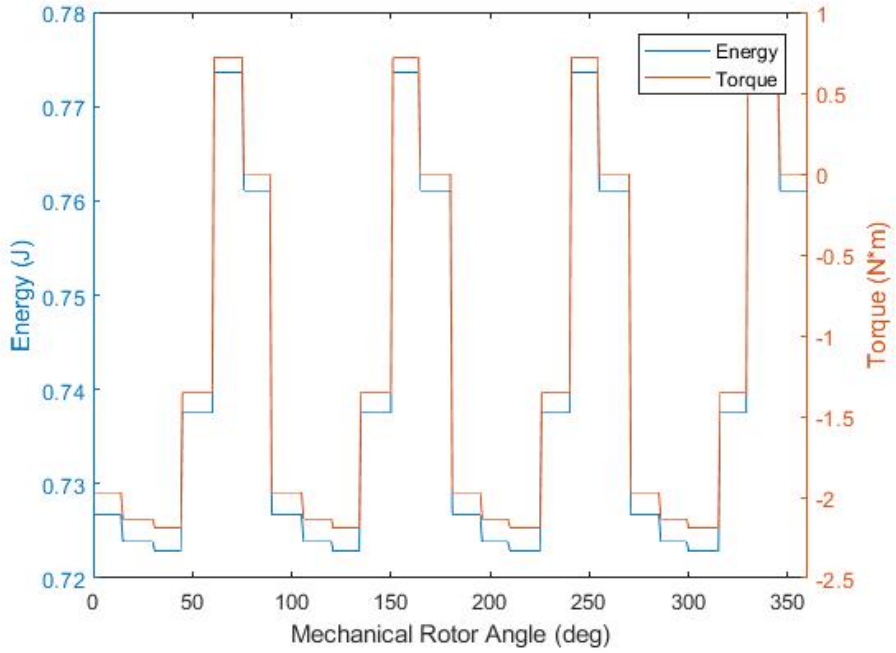

Figure 5.13: Electromagnetic torque on the drive bearing using the current machine geometry with an iron rotor

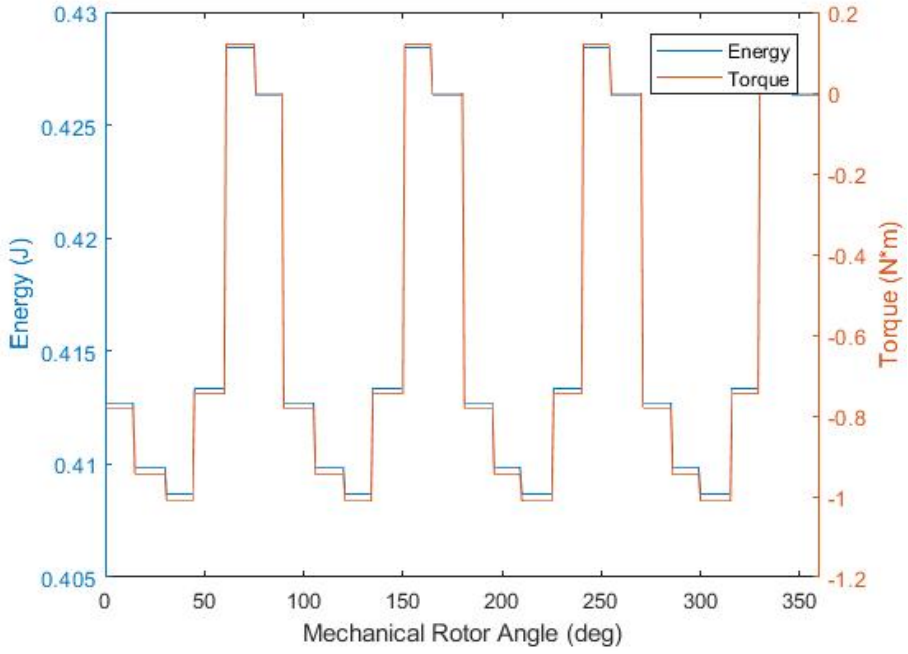

Figure 5.14: Electromagnetic torque on the drive bearing using the current machine geometry with a composite rotor

The results of the FEMM simulation show the same pattern in the torque up to 30°, but the magnitude and direction of the torque is different after 30°. It is believed that part of this error is the propagation of the difference between the flux density of the dynamic model and FEMM noted at the end the last section. It should also be noted that the FEA results conflict with the intuition developed for the machine as the torque is always in the clockwise direction. This could be due to the method used to calculate the torque and should be checked against another FEA simulation software such as ANSYS®

Also, the scaling of torque with k_{com} needs to be considered. Using the approximation of k_{com} represented in (2.28), the value of k_{com} is 1 in the interpole region. For this composite and geometry, k_{com} is equal to 0.15 under the pole face. The torque production is expected to scale with the k_{com} under the pole face. The FEMM results indicates that the torque production is proportional to a k_{com} of about 0.3 which is the k_{com} indicated by the FEM results in the last section. The torque values from FEMM verify this scaling and are shown in Table 5.4.

Verification using FEA indicates that it is possible to use the composite loss factor to incorporate the effects of composite materials into an ideal force model with an acceptable level of confidence. The primary concern of the model is to predict forces

Table 5.4: FEMM torque predictions about (0,0) with the electrical angle increasing in a clockwise direction

Electrical Angle (deg)	Torque (N*m)
Iron Rotor	
0°	-2.075
15°	-2.106
30°	-2.130
45°	-2.129
60°	-2.128
75°	-2.102
Composite Rotor	
0°	-0.537
15°	-0.540
30°	-0.549
45°	-0.551
60°	-0.553
75°	-0.549

and torque values with enough accuracy to develop control algorithms and to aid in the development of a HSFESS. The FEA results indicate that the torque model needs further verification before there is enough confidence in the model. The analytical results make more intuitive sense, but the machine must be operational before the model is fully validated.

Chapter 6

Summary and Recommendations

6.1 Summary

NASA's goal of developing an energy storage system to aid in lunar colonization is dependent on high energy storage density. A flywheel energy storage system is best suited for this application. It is the goal of the interdisciplinary team of engineers and physicists at the University of Idaho to aid NASA in the development of such a device.

As (1.1) shows, the energy stored in a flywheel is proportional to the square of the speed while it is only linearly proportional to the moment of inertia. Therefore, it is more advantageous to increase the speed of the flywheel.

The first design phase of this project resulted in an inside-out field regulated reluctance machine for the UIFESS. This poses a problem for the development of a high speed FESS, as the air gap is a critical component to the control of the device. As the machine speed is increased, the rotor stresses increase exponentially, and the deflection will increase. This indicates that high strength materials is needed to develop a HSFESS in the configuration of the UIFESS.

As is the case with all engineering challenges, there is a trade off when selecting materials for a HSFESS. This represents itself as a balance between cost, strength, and permeability. For the material to be useful in a machine, it needs to have a sufficiently high permeability to facilitate magnetic interaction.

Previous modeling approaches often assume ideal material properties to simplify the analytical approach. This is often acceptable because machines are often designed using materials with very high relative permeabilities. This is not a valid assumption when working with most high strength materials, like composites, because there permeabilities are often much lower than materials like iron.

Through the development of a composite loss factor that is a function of the materials used in the machine design, it is now possible to produce initial estimates of the machine capabilities when considering non-ideal materials. Also, using FEMM results, it is possible to develop accurate models using ideal equations and the composite loss factor to simulate machine dynamics.

Another challenge of developing a HSFESS is that the machine is being operated close to its functional limits. This makes it important to account for saturation and iron effects on the air gap permeability. By determining the machine's position along the saturation curve using the MMF already being calculated, it is possible to map the

effects of saturation to an effective air gap. It is also possible to map the effects of iron on the air gap permeability to the effective air gap. These effects will propagate through the model and be reflected in force and torque calculations.

Due to the expense of developing machines, it is desirable to have the capability to model many machine configurations to optimize the design before any hardware is developed. This is possible with relatively little effort by developing the model in a modular fashion.

A modular model can be developed by defining the interactions between the system components as functions of the component properties. Then, by updating the component properties, the system interactions will be updated to reflect the new configuration. This is achievable with the support of software packages like MATLAB®, Simulink®, and even Python™.

6.2 Future Work

This body of work attempts to quantify the effects of non-ideal materials and saturation on the dynamics of a field regulated reluctance machine and to present a methodology for a modular modeling approach to assist in the design and control of a HSFESS.

Now that the effect of the non-ideal materials has been defined, the models in [5] can be revisited to select an optimal rotor configuration. The optimal rotor configuration in terms of both mechanical and electromagnetic properties will likely have a slope from the edge of the pole face to the edge of the interpole region that is not set under the pole face. The models in [5] will also provide an estimate for the deformation of the rotor with respect to the angular velocity. That displacement can be fed back to the effective air gap to determine the effect on the forces and torque produced by the machine. In this way, the deformation of the rotor can be fed back into the control system design.

The mutual inductance method of calculating torque should be compared with the FEMM results to determine if the error is due to the energy calculation or the turns function. The development of some control law is needed to maintain the electrical angle with respect to the mechanical angle to provide a motoring simulation. These will likely be addressed in Brian Peterson's dissertation [20].

In order to correct for the error on the boundary of the pole face and interpole region, k_{com} can be multiplied by a weighting function to reduce its effect on the flux density, computed for the boundary between the pole face and inter-pole regions. The weighting function could be defined using a Fourier series tuned to the rotor and stator geometry using FEA to select the appropriate frequencies.

Also, mentioned in [5] is the need for the development of a non-rigid model for the rotor due to the changing radius. This will allow for the prediction of the changes to the rotor's moment of inertia which will impact the machine stability. This will also improve the prediction of the rotor deformation in regard to the air gap which will affect the electromagnetic properties of the machine.

One possible solution to non-rigid modeling is to identify the dominant modes of the non-rigid system and model the system as a series of systems that transition at specific rotational frequencies. This model scheduling can be incorporated with a controller gain scheduling scheme to develop a system of systems that transition as a function of rotational speed.

It would also be beneficial to revisit saturation in the context of a composite rotor. In [10], there are methods described to determine the effective B-H curve caused by the interaction of multiple permeabilities. This is evident in the FEMM models that the use of a composite rotor/floater results in less saturation of the iron. This also makes intuitive sense when considering (2.6).

Also, it would be beneficial to combine this work with the work of [2] to incorporate the effects of rotor distortion, saturation, and non-ideal materials into the translational force calculations. In [2], there is also a discussion on incorporating axial air gap distortions into the model. Combining the torque production model with axial air gap distortions will allow the model to simulate the effects of a tilted rotor. This inclusion will be important in the development of high performance control schemes.

In order to better model the current through the coil, the inductance and resistance of the coils should be included in the model to represent the actual current in the coils as a function of time. Depending on where the controller is designed in the system, the power electronics should also be incorporated into the model. This will allow the inclusion of any delay between command, a signal issued from the controller, and actuation, the h-bridge circuits changing state and the current reaching the desired goal.

After completing the aforementioned tasks, the model can be converted to Simulink® to model the systems electrical and mechanical dynamics in a real time solver. Also, using ANSYS® the electromagnetic profile, torque, and bearing forces can be verified, especially when considering composite rotors. This will be greatly beneficial to those who are developing control schemes for the HSFESS. Also, this model can be used to perform system identification, without risking damage to the machine, to develop a transfer function that can be used for controls development.

Aside from modeling and control of a HSFESS, the work of Kevin Ramus [4] will need to be revisited to improve the switching capability of the power electronics.

This will involve a significant study of electromagnetic interference, as the future power electronics will have much higher switching capabilities.

References

[1] C. Warner, Ed. (2018). Nasa outlines new lunar science, human exploration missions, [Online]. Available: https://www.nasa.gov/feature/nasa-outlines-new-lunar-science-human-exploration-missions.

[2] B. T. Wimer, "Dynamic model and design of an integrated flywheel energy storage system," Thesis, University of Idaho, May 2014.

[3] B. A. Kisling, "Active magnetic bearing control for an experimental flywheel energy storage system," Thesis, University of Idaho, May 2014.

[4] K. R. Ramus, "Power electronic components and hardware for an experimental flywheel energy storage system," Thesis, University of Idaho, May 2014.

[5] J. D. Pettingill, "Multi-physic stochastic modeling of a high speed composite flywheel energy storage system," Thesis, University of Idaho, May 2016.

[6] B. F. Kaschmitter, "Modeling, design, and optimization of a high-speed flywheel for and energy storage system," Thesis, University of Idaho, May 2017.

[7] J. J. Wolmerans, M. Geest, H. Polinder, J. A. Ferrreira, and D. Zeilstra, "Composite materials for low loss rotor construction," *IEEE Inter. Electric Machines and Drives Conf.*, pp. 295–299, 2011.

[8] S. Koch, M. Peter, and J. Fleischer, "Lightweight design and manufacturing of composites for high-performance electric motors," *1st Cirp Conf. on Composite Material Parts Manufacturing*, pp. 283–288, 2017.

[9] Y. Guo, J. Zhu, and D. G. Dorrell, "Design and analysis of a claw pole permanent magnet motor with molded soft magnetic composite core," *IEEE Trans. On Magnetics*, vol. 45, no. 10, pp. 4582–4585, 2009.

[10] T. A. Lipo, *Introduction to AC Machine Design*. Wiley-IEEE, 2017.

[11] O. Misir, F. Dobbert, and B. Ponick, "Analytical method for the air gap permeance calculation of salient pole synchronous machines," *Elektrotechnik und Informationstechnik*, vol. 133, no. 2, pp. 103–111, 2016.

[12] T. Lubin, T. Hamiti, H. Raik, and A. Rezzoug, "Comparison between finite-element analysis and winding function theory for inductances and torque calculation of a sychronous reluctance machine," *IEEE Trans. On Magnetics*, vol. 43, no. 8, pp. 3406–3401, 2007.

[13] J. C. Moreira and T. A. Lipo, "Modeling of saturated ac machines including air gap flux harmonic components," *IEEE Trans. On Industry Applications*, vol. 28, no. 2, pp. 343–349, Mar. 1992.

[14] P. Kundur, *Power System Stability and Control*. McGraw-Hill, 1994.

[15] H. Bleuler, M. Cole, P. Keogh, R. Larsonneur, E. Maslen, R. Nordmann, Y. Okada, G. Schweitzer, and A. Traxler, *Magnetic Bearings: Theory, Design, and Application to Rotating Machinery*. Springer, 2009.

[16] L. N. Hand and J. D. Finch, *Analytical Mechanics*. Cambridge University Press, 1998.

[17] D. C. Hamill, "Lumped equivalent circuits of magnetic components: The gyrator-capacitor approach," *IEEE Trans. Power Electron.,*, vol. 8, no. 2, pp. 97–103, Apr. 1993.

[18] N. A. Al-Nuaim and H. A. Toliyat, "A novel method for modeling dynamic air-gap eccentricity in synchronous machines based on modified winding function theory," *IEEE Trans. On Energy Conversion*, vol. 13, no. 2, pp. 156–162, Jun. 1998.

[19] A. E. Fitzgerald, J. C. Kingsley, and S. D. Umans, *Electric Machinery*, 6th ed. McGraw-Hill, 2003.

[20] B. Peterson, "Model identification adaptive control of a field regulated reluctance machine applied to an experimental flywheel energy storage system," Dissertation, University of Idaho, to be published.

[21] D. C. Meeker, *Finite element method magnetics*, version 4.2, 2016. [Online]. Available: http://www.femm.info.

Appendix

Matlab Code for Dynamic Modular Model

Machine Torque

```
clear all
close all
clc

sample_f=1*10^5;
res = 1/sample_f;

mu_0 = 4*pi*10^-7; %henries/meter

%theta = 0:res:2*pi; %radians

theta = linspace(0,2*pi,sample_f);

FRRMRotorParameters
FRRMStatorParameters

h_e = 2*0.0254;%min([h_e_rotor,h_e_stator]);

%LZY_Susan_decel = -12; %rad/s^2

LZY_Susan_decel = 0;%-11; %rad/s^2

k_com = 1;

%% Coil Order
% 1 2 3 4 5 6 7 8 9 10 11 12 13 14 15 16 17 18 19 20 21 22 23 24
% Q Q D D D D Q Q D D D D Q Q D D D D Q Q D D D D

I_d = 1.75; %Amps
```

```
30 I_q = 0.952*I_d; %Amps
31
32 I = [I_q I_d I_d I_d I_d I_q I_q I_d I_d I_d...
33           I_d I_q I_q I_d I_d I_d I_d I_q I_q I_d I_d I_d
                I_d I_q];
34
35 %% Define the effective air gap
36
37 gap_e = effective_gap_function( theta, ...
38     stator_slot_pitch, stator_slot_opening, stator_slot_top,
           ...
39     r_stator_outer, stator_tooth_thicknes, rotor_slot_pitch,
           ...
40     rotor_pole_arc, r_rotor_pole);
41
42 gap = gap_e;
43
44 gap_avg = (1/(2*pi))*trapz(theta,gap,2); %meters
45
46 gap_inv = gap.^-1;
47
48 gap_inv_avg = (1/(2*pi))*trapz(theta,gap_inv,2);
49
50 %% Define the composite loss factor
51
52 k_com = zeros(1,length(theta));
53 mu_c = 30;
54 mu_fe = 1616;
55 lfe = 2*(stator_slot_depth)+rotor_slot_pitch*(r_stator_mid);
56 lc = 2*(r_rotor_mid-r_rotor_pole)+rotor_slot_pitch*(
       r_rotor_mid);
57 for i = 1:length(theta)
58     if(gap(i) <= gap(1))
59         k_com(i) = ((lfe/mu_fe) + gap(1))./((lfe/mu_fe) +
               gap(1) +...
60                (lc/mu_c));
```

```
61      else
62          k_com(i) = 1;
63      end
64  end
65
66
67  %% Define the turns function as a matrix for faster
        computation.
68
69  turns = turns_function(theta,num_slot,num_coil_per_slot,...
70      coil_turns,stator_slot_pitch);
71
72  % Calculate the average of the turns functions by each coil.
73  turns_avg = (1/(2*pi))*trapz(theta,turns,2); %
74
75
76  %% Define the modified winding fuction as a matrix.
77
78  m_winding = modified_winding_function(theta,res,num_slot,
        turns...
79      ,gap_inv_avg,gap_inv);
80
81
82  %% Calculate MMF from each coil.
83
84  mmf = mmf_function(theta, num_slot, m_winding, I);
85  mmfc = mmf.*k_com;
86
87  %% Solve for B
88  H = mmf.*gap_inv;
89  Bfe = H*mu_0;
90
91  H = mmfc.*gap_inv;
92  Bc = H*mu_0;
93
94  % import FEMM data.
```

```
95  filename = ...
96  'E:\David Arnett\flywheel\FEMM\
        DriveBearing_Iron_B_LinePlot_360_e0.txt';
97  startRow = 3;
98
99  BfeFEMM = importFEMMdata(filename, startRow);
100
101 filename = ...
102 'E:\David Arnett\flywheel\FEMM\
        DriveBearing_Composite_B_LinePlot_360_e0.txt';
103 startRow = 3;
104
105 BcFEMM = importFEMMdata(filename, startRow);
106
107 %%{
108 figure('Name',['Flux Density with Electrical Angle of ' 0 '
        Degrees'])
109
110     % Create plot
111     yyaxis left
112     plot(theta,Bfe,'DisplayName','B_{fe}');
113     hold on
114     plot(theta,BfeFEMM,'DisplayName','B_{fe} from FEMM');
115     hold off
116
117     % Create ylabel
118     ylabel('Flux Density (T)');
119
120     yyaxis right
121     plot(theta, gap_inv,'DisplayName','Inverse air gap','
            LineStyle',...
122         ':','Color',[0 0 0]);
123     % Create ylabel
124     ylabel('gap^{-1} (m)');
125     ylim([0 1300]);
126     % Create xlabel
```

```
127     xlabel('Electrical Angle (theta)');
128
129     % Create limits of the axes
130     xlim([0 6.2832]);
131
132     legend('show')
133 %}
134
135
136
137 %% Solve for energy in the airgap
138
139 energy = zeros(1,361);
140 for alpha = 0:360
141
142     theta_m = 0;
143     theta_e = alpha;
144
145     [energy(alpha+1), mmf_plot, gap_plot] = ...
146         energy_function(theta,res,theta_e,theta_m,mu_0,
                num_slot,h_e,...
147             r_stator_outer,gap,m_winding,I,k_com);
148
149 end
150
151 %% Solve for torque
152
153 diftorque = diff(energy)/deg2rad(1);
154 diftorque = [diftorque(90) diftorque];
155
156 torque = zeros(1,361);
157
158 for alpha = 0:360
159     torque(alpha+1) = sum(diftorque(1:alpha+1));
160 end
161
```

```
%FEMM Torque


alpha = 0:360;

%%{
figure('Name','Air gap Energy and Torque')

% Create plot
      yyaxis right
      plot(alpha, torque);
      % Create ylabel
      ylabel('Torque (N*m)');
      %ylim([-10 10]);

      yyaxis left
      plot(alpha, energy);
      % Create ylabel
      % Create ylabel
      ylabel('Energy (J)');
      %ylim([-1500 1500]);

      % Create xlabel
      xlabel('Mechanical Rotor Angle (deg)');

      % Create x-limits of the axes
      xlim([0 360]);

      legend('Torque', 'Energy');
%}

%% Solve for acceleration

I_ozG = 0.119014; %kg*m^2

ang_acel = torque/I_ozG; %rad/s^2
```

Rotor Parameters

```
%———————— FRRM Rotor Parametors ————————%

%——— Material Properties ———%

%Permeability - Assuming a single radial material, if the material changes
%radialy consider using FEM to find an effective permeability
mu_rotor = 1616; %Electric Steel


%——— Geometry ———%

r_rotor_pole = 0.0674878;   %meters
r_rotor_outer = 0.09525;    %meters
r_rotor_inner = 0.077851;   %meters
r_rotor_mid = r_rotor_inner + ((r_rotor_outer - r_rotor_inner)/2); %meters

h_rotor = 0.0508;           %meters
rotor_stacking_factor = 0.96;
h_e_rotor = h_rotor*rotor_stacking_factor;

rotor_slot_pitch = 1.5708;   %radians
rotor_slot_opening = 1.0472; %radians
rotor_pole_arc = 0.523599;   %radians

num_pole = 4;
```

Stator Parameters

```
%———————— FRRM Stator Parametors ————————%

%——— Material Properties ———%

%Permeability
mu_stator = 1616; %Electric Steel


%——— Geometry ———%

r_stator_outer = 0.0664972;          %meters
r_stator_tooth_cap = 0.0644906;      %meters
r_stator_tooth_neck = 0.062484;      %meters
r_stator_mid = 0.0254;

stator_tooth_thicknes = r_stator_outer - r_stator_tooth_cap;
stator_tooth_taper_thicknes = r_stator_tooth_cap -
    r_stator_tooth_neck;

h_stator = 0.0508;                   %meters
stator_stacking_factor = 0.96;
h_e_stator = h_stator*stator_stacking_factor;

stator_slot_pitch = 0.261799;        %radians
stator_slot_opening = 0.1747;        %radians
stator_slot_top = 0.0116078;         %meters
stator_slot_bottom = 0.0032004;      %meters
stator_slot_depth = 0.0322072;       %meters



num_slot = 24;
coil_turns = 55;
num_coil_per_slot = 2;
```

Effective Air Gap

```
function [ gap_e ] = effective_gap_function( theta, ...
    stator_slot_pitch, stator_slot_opening, stator_slot_top, ...
    r_stator_outer, stator_tooth_thicknes, rotor_slot_pitch, ...
    rotor_pole_arc, r_rotor_pole)
%UNTITLED3 Summary of this function goes here
%   Detailed explanation goes here

%% Effective Air Gap
    %theta is the angular position of the rotor with respect to the winding
    %reference

    %alpha is a particular position along the stator inner surface

    gap_0 = r_rotor_pole - r_stator_outer;

    gap_r = zeros(1,length(theta));

    alpha_rp = rotor_slot_pitch;

    e1 = rotor_pole_arc/2;
    e2 = alpha_rp/2;
    e3 = alpha_rp - rotor_pole_arc/2;
    e4 = alpha_rp;

    for i=1:length(theta)
        theta_m = theta(i);

        while(theta_m < 0)
            theta_m = theta_m + alpha_rp;
        end
```

```
31
32          while(theta_m >= alpha_rp)
33              theta_m = theta_m - alpha_rp;
34          end
35
36          if( (theta_m >= 0) &&...
37                  (theta_m < e1) )
38
39              gap_r(i) = gap_0;
40
41          elseif( (theta_m >= e1) &&...
42                  (theta_m < e2) )
43
44              gap_r(i) = gap_0 + (pi/2)*r_rotor_pole*(theta_m -
                    e1);
45
46          elseif( (theta_m >= e2) &&...
47                  (theta_m < e3) )
48
49              gap_r(i) = gap_0 + (pi/2)*r_rotor_pole*(e4 - e1 -
                    theta_m);
50
51          elseif( (r_rotor_pole*theta_m >= e3) &&...
52                  (r_rotor_pole*theta_m < e4) )
53
54              gap_r(i) = gap_0;
55
56          else
57              gap_r(i) = gap_0;
58          end
59      end
60
61
62      b0 = (stator_slot_opening*r_stator_outer);
63      stator_tooth_width = ((stator_slot_pitch*r_stator_outer)
          ...
```

```
64          - (stator_slot_opening*r_stator_outer));
65      e1 = stator_tooth_width/2;
66      e2 = (e1 + stator_tooth_thicknes);
67      e3 = (e2 + ((b0/2)-stator_tooth_thicknes));
68      e4 = (e3 + ((b0/2)-stator_tooth_thicknes));
69      e5 = (e4 + stator_tooth_thicknes);
70      e6 = (stator_slot_pitch*r_stator_outer);
71      alpha_sp = stator_slot_pitch;
72
73      gamma = pi/2 - atan(stator_tooth_thicknes/...
74          ((stator_slot_top - (stator_slot_opening*
                r_stator_outer)))/2);
75
76      gap_s = zeros(1,length(theta));
77
78      for i=1:length(theta)
79          theta_m = theta(i);
80
81          while(theta_m < 0)
82              theta_m = theta_m + alpha_sp;
83          end
84
85          while(theta_m >= alpha_sp)
86              theta_m = theta_m - alpha_sp;
87          end
88
89          if( (r_rotor_pole*theta_m >= 0) &&...
90                  (r_rotor_pole*theta_m < e1) )
91
92              gap_s(i) = 0;
93
94          elseif( (r_rotor_pole*theta_m >= e1) &&...
95                  (r_rotor_pole*theta_m < e2) )
96
97              gap_s(i) = (pi/2)*(r_rotor_pole*theta_m - e1);
98
```

```
99          elseif( (r_rotor_pole*theta_m >= e2) &&...
100                 (r_rotor_pole*theta_m < e3) )
101
102             gap_s(i) = (pi/2)*(r_rotor_pole*theta_m - e1) + ...
103                 gamma*(r_rotor_pole*theta_m - e2);
104
105         elseif( (r_rotor_pole*theta_m >= e3) &&...
106                 (r_rotor_pole*theta_m < e4) )
107
108             gap_s(i) = (pi/2)*(e5 - r_rotor_pole*theta_m) + ...
109                 gamma*(e4 - r_rotor_pole*theta_m);
110
111         elseif( (r_rotor_pole*theta_m >= e4) &&...
112                 (r_rotor_pole*theta_m < e5) )
113
114             gap_s(i) = (pi/2)*(e5 - r_rotor_pole*theta_m);
115
116
117         elseif( (r_rotor_pole*theta_m >= e5) &&...
118                 (r_rotor_pole*theta_m < e6) )
119
120             gap_s(i) = 0;
121
122         else
123             gap_s(i) = 0;
124         end
125     end
126
127     gap_e = gap_r + gap_s;
128
129
130 end
```

Turns Function

```
function [turns] = turns_function(theta,Coils,Coils_per_slot
    ,Turns,Beta)
%UNTITLED4 Summary of this function goes here
%   Detailed explanation goes here

    Turns_e = Turns*Coils_per_slot;

    turns = zeros(Coils,length(theta));
%%{
    for x = 1:Coils
        if (x-1) <= 15
            for i = 1:length(theta)
                if (theta(i) >= (Beta/2 + 2*Beta + (x-1)*
                    Beta)) &&...
                        (theta(i) < (Beta/2 + 8*Beta + (x-1)
                            *Beta))
                    turns(x,i) = Turns_e;
                else
                    turns(x,i) = 0;
                end
            end
        elseif (x) >= 22
            for i = 1:length(theta)
                if (theta(i) >= (Beta/2 + ((x-1)-22)*Beta))
                    &&...
                        (theta(i) < (Beta/2 + 6*Beta + ((x
                            -1)-22)*Beta))
                    turns(x,i) = Turns_e;
                else
                    turns(x,i) = 0;
                end
            end
        else
            for i = 1:length(theta)
```

```
30                  if (theta(i) > (Beta/2 + ((x-1)-16)*Beta))
                       &&...
31                          (theta(i) < (Beta/2 + 18*Beta + ((x
                               -1)-16)*Beta))
32                      turns(x,i) = 0;
33                  else
34                      turns(x,i) = Turns_e;
35                  end
36              end
37          end
38
39          if (x-1) == 6 || (x-1) == 7 || (x-1) == 8 || (x-1)
               == 9 ||...
40                  (x-1) == 10 || (x-1) == 11 || (x-1) == 18 ||
                       ...
41                  (x-1) == 19 || (x-1) == 20 || (x-1) == 21 ||
                       ...
42                  (x-1) == 22 || (x-1) == 23
43              turns(x,:) = turns(x,:)*-1;
44          end
45      end
46 %}
47 end
```

Modified Winding Function

```
function [m_winding] = modified_winding_function( theta, res
    , num_slot,...
     turns, gap_inv_avg, gap_inv )
%UNTITLED5 Summary of this function goes here
%   Detailed explanation goes here
    m_winding = zeros(num_slot,length(theta));

    for x = 1:num_slot
        m_winding(x,:) = turns(x,:)-(1/(2*pi*gap_inv_avg))...
            *(trapz(theta, gap_inv.*turns(x,:),2));
    end
end
```

MMF

```
function [mmf_total] = mmf_function(theta, Coils, Winding, I
    )
%MMF Calculate MMF from each coil
%   Detailed explanation goes here

    mmf = zeros(Coils,length(theta));

    mmf = I.'.*Winding;

    mmf_total = sum(mmf);

end
```

Air Gap Energy

```
function [ energy, mmf, gap ] = energy_function(theta,res,
    theta_e,theta_m,mu_0,num_slot,h,r,gap,Winding,I,k_com)
%UNTITLED Summary of this function goes here
%   Detailed explanation goes here
%   theta_e -> electrical shift
%   theta_m -> mechanical shift

    %% Handle mechanical shift
    alpha_m = deg2rad(theta_m);

    while alpha_m > 2*pi
        alpha_m = alpha_m - 2*pi;
    end

    while alpha_m < 0
        alpha_m = alpha_m + 2*pi;
    end

    [dif,shift] = min(abs(theta-alpha_m));
    gap = circshift(gap, shift); %meters

    gap_inv = gap.^-1;

    %% Handle electrical shift
    alpha_e = deg2rad(theta_e);

    edges = 0:0.2618:6.2832;
    deg2coil = discretize(theta,edges);

    while alpha_e > 2*pi
        alpha_e = alpha_e - 2*pi;
    end

    while alpha_e < 0
```

```
34          alpha_e = alpha_e + 2*pi;
35      end
36
37      [dif,index] = min(abs(theta-alpha_e));
38      I_shift = deg2coil(index);
39      I = circshift(I, I_shift);
40
41      mmf = mmf_function(theta, num_slot, Winding, I);
42
43      mmf = mmf.*k_com;
44
45      %% Calculate energy
46      energy = ((h * mu_0) / 4) *...
47          (trapz(theta,((2*r.*(mmf.^2)).*gap_inv),2) +...
48          (trapz(theta,(mmf.^2),2)));
49
50  end
```